ADVANCED FUNCTIONAL MATERIALS
www.afm-journal.de

Materials Views
www.MaterialsViews.com

Domain Wall Conduction and Polarization-Mediated Transport in Ferroelectrics

Rama K. Vasudevan, Weida Wu, Jeffrey R. Guest, Arthur P. Baddorf,*
*Anna N. Morozovska, Eugene A. Eliseev, Nina Balke, V. Nagarajan,**
Peter Maksymovych, and Sergei V. Kalinin*

Nanometer-scale electronic transport in engineered interfaces in ferroelectrics, such as domains and topological defects, has emerged as a topic of broad interest due to potential applications in information storage, sensors and photovoltaic devices. Scanning probe microscopy (SPM) methods led to rapid growth in the field by enabling correlation of the unique functional properties with microstructural features in the aforementioned highly localized phenomena. In addition to conduction localized at interfaces, polarization-mediated control of conduction through domains in nanoscale ferroelectrics suggests significant potential for use in memristor technologies. In parallel with experiment, theory based on thermodynamic Landau-Ginzburg-Devonshire (LGD) framework has seen rapid development, both rationalizing the observations, and hinting at possibilities for local, deterministic control of order parameters. These theories can successfully account for static interface conductivity at charged, nominally uncharged and topologically protected domain walls. Here, recent experimental and theoretical progress in SPM-motivated studies on domain wall conduction in both standard and improper ferroelectrics are reviewed. SPM studies on transport through ferroelectrics reveal that both domains and topological defects in oxides can be exploited as individual elements for use in functional nanoscale devices. Future prospects of the field are discussed.

1. Introduction

Topological defects are one of the traditional objects of study and fascination in physics in areas as dissimilar as cosmology,[1] soft matter,[2] and ferroic systems.[3,4] Examples include domain walls in ferroics, vortices in superconductors,[5] defects in topological insulators,[6] ordered point defect structures,[7,8] liquid crystalline matter,[9] and many others. In many cases, the functionality of macroscopic materials are determined by the properties of topological defects, e.g., magnetization or polarization dynamics in ferroics and transport in superconductors. Furthermore, observations and studies of topological defects provide fundamental insight into the physical properties of the system, including the nature of order parameter and associated free energies. In recent years, topological defects were recognized as a powerful paradigm for nanoscale device engineering due to the combination of unique physical properties and capability for manipulation by external magnetic, electric, or strain fields without the disruption of the host lattice.[10] This has led to conceptualization of a broad spectrum of reconfigurable magnetoelectric, optoelectonic, and strain-coupled memory and logic devices simply through the creation and manipulation of topological defects.[11–16]

In ferroics, materials properties and functionality are often defined by collective symmetry breaking distortions giving rise to order parameter fields. The regions with dissimilar order parameters orientations are necessarily separated by topological defects, resulting in domain structures and domain walls. Theoretical predictions and experimental discoveries of novel functionalities emerging at domain walls in ferroelectrics and ferroelastic materials as well as the emergence of scanning probe microscopy methods has led to the recent spate of investigations of topological defects in these systems. These are associated with either intrinsic symmetry-related effects on electronic and phonon structure, or interactions between ferroic system and other materials functionalities, including coupling to other order parameters, semiconducting and electrochemical properties. The initial work by Lajzerowicz and Niez[17] is foundational in this regard, for they showed the possibility of domain walls undergoing phase transitions while the domains themselves did not. The original theoretical studies of ferroelectric

---

R. K. Vasudevan, Prof. V. Nagarajan
University of New South Wales
Kensington, 2052, Australia
E-mail: nagarajan@unsw.edu.au

Prof. W. Wu
Department of Physics and Astronomy and
Rutgers-Centerfor Emergent Materials
Rutgers University
Piscataway, NJ 08854, USA
E-mail: wdwu@physics.rutgers.edu

Dr. J. R. Guest
Center for Nanoscale Materials
Argonne National Laboratory
Argonne, IL 60439, USA

Dr. A. N. Morozovska
Institute of Physics
National Academy of Sciences of Ukraine

Dr. E. A. Eliseev
Institute for Problems of Material Science
National Academy of Sciences of Ukraine
Kiev, Ukraine

Prof. S. V. Kalinin, Dr. A. P. Baddorf, Dr. N. Balke, Dr. P. Maksymovych
The Center for Nanophase Materials Sciences
Oak Ridge National Laboratory
Oak Ridge, TN 37831, USA
E-mail: maksymovychp@ornl.gov

DOI: 10.1002/adfm.201300085

domain walls by Guro et al.[18] explored the effects of the polarization charge on the local carrier distributions, i.e., coupling between ferroelectricity and semiconducting properties of material manifesting at the domain walls. One of the predictions of the work by Guro et al. was the metallic conductivity at ferroelectric domain walls, which took almost 40 years to demonstrate experimentally.[19,20] Recently, semiconducting phenomena at uniaxial domain walls was explored in more detail by Tagantsev[21,22] and Morozovska.[23–25]

Many ferroelectric materials are also ferroelastic, implying complex interplay between polarization and strain effects. Similarly, in materials with several competing order parameters multiple new functionalities can emerge at domain walls.[11] A significant body of work explored the structure of ferroelectric domain walls in presence of such coupling, predicting unusual polarization rotations at the domains walls. Strain coupling can significantly affect semiconducting behavior at domain walls.[24] Conversely, in ferroelastic materials coupling between two order parameters can give rise to domain wall ferroelectricity.[26–28] In systems with magnetic and ferroelectric orders, magnetoelectric coupling,[29] and magnetic phase transitions[30] were predicted. Finally, strong strain dependence of electrochemical phenomena allowed a set of predictions on ionic phenomena at domain walls.[31,32]

A novel set of mechanisms emerge at the atomistic level. As explored by Gemming et al.,[33] local increase of symmetry at the domain wall can stabilize a high-temperature phase. For those materials that possess a ferroic phase transition associated with a metal-insulator transition, this can give rise to changes in local conductivity.[30] Finally, it is important to note that formation of domain structures in ferroelastics can also give rise to mesoscopic strains and mesoscopic regions of metallic regions following the morphology of the domain walls, as observed in VO_2.[34]

2. Enabling Instrumentation

While the role of topological defects in functionality of ferroics and the emergence of novel phenomena at the defects has been recognized for over half a century,[18] experimental studies have been limited. Indeed, macroscopic samples typically contain multiple topological and other defects, precluding unambiguous determination of properties of each. The progress was achieved due to the synergy of progress in materials synthesis, enabling samples with (relatively) low defect densities,[35] and development of local techniques based on scanning probe microscopy[36–39] (SPM) that enabled domain structures to be visualized, and the properties of the individual topological[19,40,41] or structural[42,43] defect to be explored.

The approach is illustrated in **Figure 1**. Here, the SPM probe plays the role of a mobile electrode that (sequentially) establishes local electric contact to selected regions of materials surface, including the vicinity of the wall.[44,45] In parallel, electromechanical response measured at high frequency offers the insight into local polarization. Combination of this conductive AFM (cAFM)[46–48] and piezoresponse force microscopy (PFM)[49–58] data allows the spatially-resolved picture of domain structure and local conductance to be determined.[19,20,59,60]

Dr. Peter Maksymovych is a Research Staff Member at the Center for Nanophase Materials Sciences at the Oak Ridge National Laboratory. Maksymovych obtained his B.S. degree in Physical Chemistry in June 2001 from the Kiev Taras Shevchenko University, Ukraine, and a Ph.D. Degree in Physical Chemistry from the University of Pittsburgh in May 2007. He was awarded a two-year Eugene P. Wigner Fellowship from the Oak Ridge National Laboratory in 2007, followed by a continuing Staff Member appointment since 2009. His current research interests include thermoelectric energy conversion in nanoscale materials, emergent electronic properties and chemical dynamics of molecular assemblies, electron transport in ferroelectric and multiferroic materials, and electronic dynamics in molecular materials. Some of the highlights include a metal-insulator transition controlled by polarization switching in ferroelectric lead zirconate, an all-electron control of molecular assembly on metal surfaces and real-space imaging of hot-electron transport using adsorbed molecules. He is actively developing scanning probe microscopy methods which are used throughout his research. Dr. Maksymovych is an organizer of several international symposia and is a member of the American Physical and Materials Research Societies.

Nagarajan (Nagy) Valanoor received his B. Engg in Metallurgy from the University of Pune (1997) and Ph.D. from the University of Maryland (2001) under supervision of Prof. Ramesh in Materials Science and Engineering respectively. Following his Ph.D. he continued as a research associate at Maryland until 2003. He followed this with a Alexander von Humboldt Fellowship with Prof. Rainer Waser at Forschungszentrum Juliech. In 2005 he was offered a lectureship at the School of Materials Science and Engineering, where he is currently an Associate Professor and Australian Research Fellow. His research interests include understanding nanoscale phenomena in functional oxide interfaces and the synthesis of novel interfaces based on these understandings.

Weida Wu is an assistant professor at the Department of Physics and Astronomy at Rutgers University. After completing his Ph.D. in Physics at Princeton in 2004, he joined the SPM group at the University of Texas, Austin as a post-doctoral fellow until 2006. He received a NSF CAREER award in 2009, an Alexander on Humboldt Fellowship for Experienced Researcher in 2011, and a DOE Early career award in 2012. His current research focuses on nanoscale magnetism, multiferroics and correlated phenomena using state-of-the-art cryogenic SPM techniques.

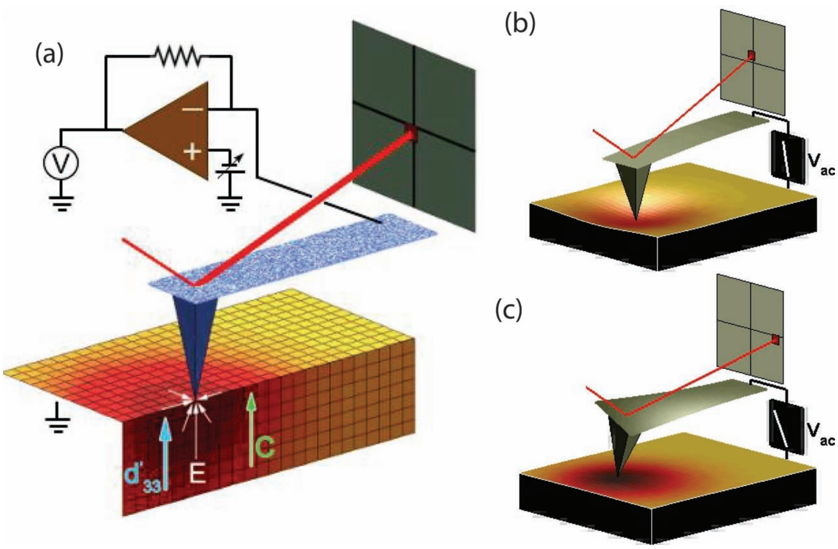

Figure 1. Schematic of conducting-AFM and PFM. a) Typically the sample is biased with the tip held at ground, and the current through the tip is read out after amplification by a current amplifier. The topography is measured by a laser/photodiode setup. Standard piezoresponse force microscopy relies on applying voltage V_{AC} to the tip and measuring b) vertical and c) lateral deflections of the cantilever, arising from piezoelectric coupling with the sample surface.

The measurements as a function of slowly-changing dc bias or time (time and voltage spectroscopies)[61] then provide insight into the bias-dependent conductance (*I–V* curve) and polarization dynamics (reversible and irreversible wall motion, domain nucleation and growth).[62–66] Note that while PFM detection is local, cAFM probes conductive path from tip-surface junction to the bottom current collecting electrode. The observed conductance in this case is determined by a resistance network that involves top, bulk and bottom interface regions of the thin film. In principle, either one of these regions can be dominant, even providing "sub-surface" contrast.

The key requirement of these measurements is establishing a high-quality electric contact between the tip and the surface. Beyond being a well-recognized problem for large band-gap semiconductors even on macroscopic scales, on the nanoscale this process is further affected by surface contamination and reactivity of oxide surfaces. These are well recognized even for the static oxide surfaces, and become particularly significant under the conditions of the high voltage stress and current flows. Notably, in many cases the field required to switch polarization in ferroelectric thin films and heterostructures[67,68] are close to that realized in electroresistive materials and devices.[69–71] Given the close similarity in defect chemistry between these materials classes, electrochemical reactivity can no longer be neglected.[72–74] In early stages, tip-induced electrochemical processes are virtually indistinguishable from polarization dynamics and exhibit presence of remanent polarization states, and hysteresis loops.[73,75,76] At later stages, irreversible deformation of surfaces and dielectric breakdown are observed,[77,78] providing experimental observables for the onset of electrochemical reactions.

Many of these stray electrochemical processes are strongly affected by surface water layer and contamination that acts as an effective catalyst for oxygen reduction/evolution reactions.[79–81] Recent studies demonstrates that imaging in the controlled glove box atmosphere or ideally in the ultrahigh vacuum (UHV) environment can greatly reduce this problem. An example of this approach is the NanoTransport system, shown in **Figure 2**. Such infrastructure, originally developed at ORNL and presently employed in several centers worldwide, is a prime example of how these advances in SPM instrumentation are critical in order to enable the precise study of such nanoscale phenomena. The NanoTransport system consists of four UHV chambers, connected by a central chamber for sample transfer under vacuum. This combination provides the ability to characterize in situ grown materials in a carefully controlled environment without exposure to air. The first chamber combines pulsed laser deposition (PLD) with differentially pumped reflection high-energy electron diffraction (RHEED), for highly controlled, layer-by-layer growth of oxide films at elevated temperatures in an oxygen atmosphere. The second chamber houses equipment for surface analysis at temperatures from 20–1800 K, including low energy electron diffraction, X-ray, and ultraviolet photoemission electron spectroscopies, employing SPECS GmBH sources and Phoibos 150 hemispherical analyzer with two-dimensional and spin detectors. The third chamber in the NanoTransport system adds an Omicron variable temperature (20–900 K) scanning tunneling/atomic force microscope (STM/AFM) for atomically resolved images of surfaces. The STM is capable of both atomic resolution imaging and tunneling spectroscopy of conducting and semiconducting oxides. An optical beam deflection detection AFM offers sensitivity for low forces in contact mode

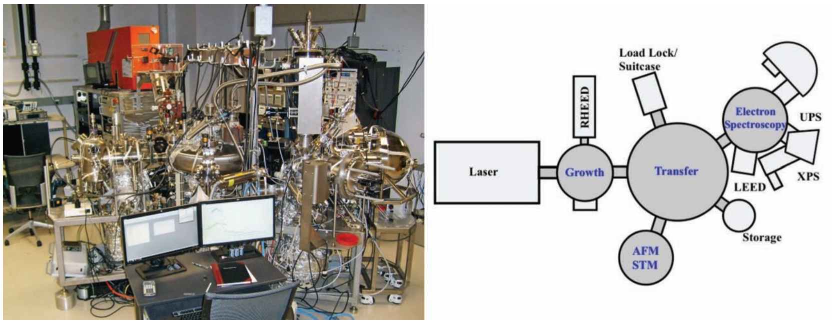

Figure 2. The NanoTransport system at Oak Ridge National Laboratory's Center for Nanophase Materials Sciences**.** The system was designed to combine growth with in situ electron spectroscopies and scanning probe microscopies. The Omicron VT-SPM has been modified to permit simultaneous PFM and c-AFM mapping and spectroscopies in a ultrahigh vacuum environment.

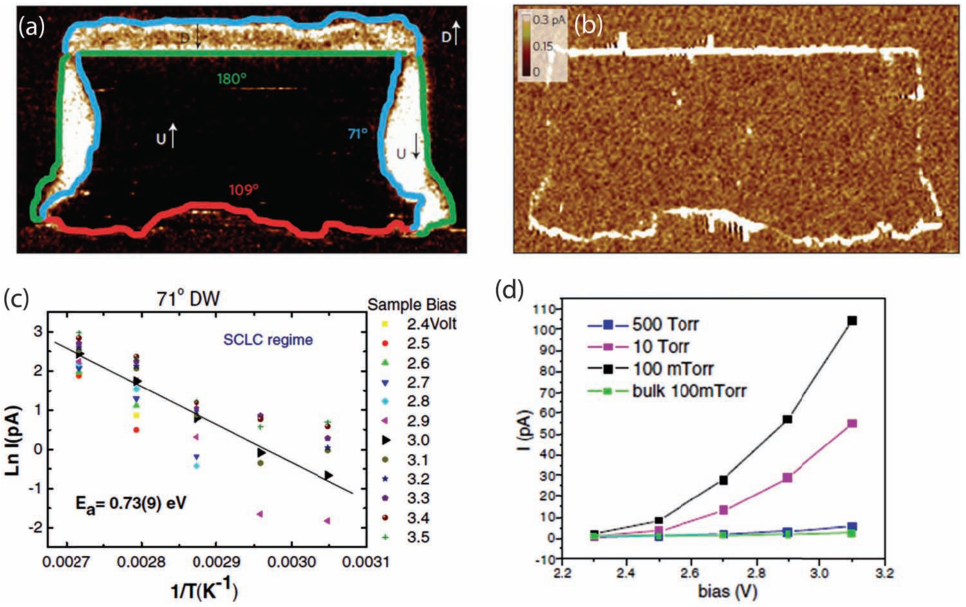

Figure 3. Static wall conduction observations. a) In-plane PFM image and b) c-AFM image showing conduction in 109° and 180° domain walls in a $BiFeO_3$thin film. Reproduced with permission.[19] Copyright 2009, Macmillan Publishers Ltd. c) Arrhenius plot of 71° domain walls. Reproduced with permission.[40] Copyright 2011, American Physical Society. d) Measurements of wall conduction as a function of cooling oxygen pressure. Reproduced with permission.[88] Copyright 2010, American Physical Society.

imaging and enables a wide array of force based measurements of local conductivity, potentials, or doping. The microscope has been modified at ORNL to a unique implementation of imaging techniques including piezoresponse force microscopy (PFM), electrochemical strain microscopy (ESM), and band excitation studies of energy dissipation.

The studies in this system have allowed to show that differences in ferroelectric and conduction values obtained in vacuum and ambient conditions arise primarily due to the ever-present water at the tip-surface interface in air. Water directly modifies material properties, through chemistry (or electrochemistry) and screening, a key factor for thin film ferroelectrics where surface water absorption has been shown to reverse polarization.[82] Furthermore, water at the tip-surface junction can modify the experimental technique, by changing the contact area and consequently effective electric field, leading to differences in observed imprint and hysteresis symmetry.[83] Finally, UHV systems allow measurements in the broad temperature range to liquid nitrogen or helium temperatures (as compared to ≈–30 °C for Peltier stages in modern ambient systems), significantly increasing the range of physical phenomena amenable to experimental exploration.

3. Direct Mapping of Wall Conductance

3.1. Static Observations

Though c-AFM was used to study domain wall conductance as early as 2003,[84] Seidel et al.[19] were the first to observe that nominally uncharged 180° and 109° domain walls in $BiFeO_3$ thin films were conductive at room temperature. This significant observation is one of the main drivers behind the interest in the novel electrical phenomena at domain walls (particularly as topological defects). At the same time, the authors found that the 71° domain walls were not conducting in their samples, as shown in **Figure 3**(a,b). Density functional theory (DFT) calculations suggested that the reason for the enhanced conductivity at the 180° and 109° domain wall could be due to several possible effects, including electrostatic potential step at the domain wall due to the (in-plane) polarization discontinuity, as well as a lowering of the band-gap due to the structural changes across the domain wall. Notably, the 71° wall showed the lowest potential step (since such a wall has no in-plane polarization discontinuity), and the smallest change in band gap, in agreement with the experimental observations.

This initial report stimulated the development of theory,[23–25,85] as well as much follow-on experimental work[20,41,86–89] to decipher the origins of the conductivity. It was soon found that domain walls and topological defects in a host of other ferroelectric materials, ranging from thin film PZT[41] to single crystal $LiNbO_3$[89] to hexagonal manganites[90,91] exhibited enhanced electrical conduction. Together, the preponderance of these studies suggests that domain wall conduction is a much more universal phenomenon than was initially believed.

In an important study, Farokhipoor et al.[40] reported studies on thin films of $BiFeO_3$ with mosaic domain structures, and found that both the 71° domain walls and the 109° walls were conducting. Crucially, temperature dependent studies (see Figure 3c) revealed that the type of conduction was qualitatively the same for both the domains and the domain walls, being governed by thermal activation of electrons from trap states at low voltages, and Schottky emission at higher voltages. It was also argued that the strain-gradient associated with the 71° and 109° ferroelastic domain wall may encourage a strain-driven segregation of oxygen vacancies at the wall, thereby lowering the Schottky barrier for surface defect states, and leading to enhanced conductivity.[92]

The role of oxygen vacancies in conduction has been further explored experimentally. In studies of La-doped $BiFeO_3$ films annealed and cooled under different oxygen pressures (thereby, resulting in varying oxygen vacancy concentrations), Seidel et al.[88] found that the conductivity at the domain wall could be modulated by over an order of magnitude, as plotted in Figure 3d. It was found that the current increased dramatically for the samples that were cooled in low oxygen partial pressures. Furthermore, temperature dependent studies by both groups have shown transport is thermally activated, with activation energies ranging from 0.24–0.5 eV[88] to 0.7 eV,[40] consistent with ionization of oxygen vacancy (defect) states.

The importance of vacancies in facilitating the conduction, then points to the reason for the widespread observation of conduction at several domain wall types in wide band-gap semiconductors: any charge which develops at the domain wall should induce accumulation or depletion/inversion of charge carriers locally. If such an accumulation or inversion is large enough, it can lead to an observable increase of static conductivity. Such theories directly posit the relationship between the magnitude of the charge at the interface, and the level of conduction, assuming the defects can migrate to neutralize the charge. Though charged walls are generally unfavorable in as-grown ferroelectrics, in hexagonal manganites, such as $HoMnO_3$[90] and $ErMnO_3$,[91] the domain walls are topologically protected, and can become highly charged depending on the specific wall orientation. Conduction-AFM studies on these improper ferroelectrics have revealed that the conduction is indeed directly correlated with the degree of charge at the domain wall. Recent work by Eng et al.[89] has further showed that the conduction at the charged walls in single crystal $LiNbO_3$ can also be modulated by excitation of carriers by light source. These studies confirm existing theories pertaining to static domain wall conductivity at charged interfaces, and furthermore show the potential for modulation of current in the spatial dimension.

Given the large reach of the interfacial conduction phenomenon, future avenues in this area include investigation of more complex interfaces (such as the phase boundaries in mixed-phase $BiFeO_3$),[93] or of completely different materials, such as core-shell perovskite structures (e.g., $BiFeO_3$-$CoFe_2O_4$), where a recent study has revealed enhanced conductivity.[60]

3.2. Wall Geometry Control

The observations of the static wall conductance offers a natural question on whether it can be deterministically controlled and modulated, a key step if domain walls are to be used as functional elements,[94,95] e.g., in nanoelectronics.[16] Long predicted relationship between wall charge and conductance[18,21,23] suggests that tuning of the conduction is possible through modulation of the charge at the interface. One approach to modulate the charge profile along an individual domain walls is to write (by a biased SPM tip) a domain with predefined orientation, thus controlling the polarization discontinuity. The domain walls can develop anisotropic spatial charge even if the written walls are initially uncharged, either due to polarization dynamics at the domain wall (that vary due to inhomogeneous strain fields around the ring-type structure),[96] or due to intrinsic effects such as angle-dependent electrostriction and flexoelectric coupling mechanisms.[25] In either case, the requirement for geometrical tunability is for a polarization discontinuity to vary as a function of wall angle.

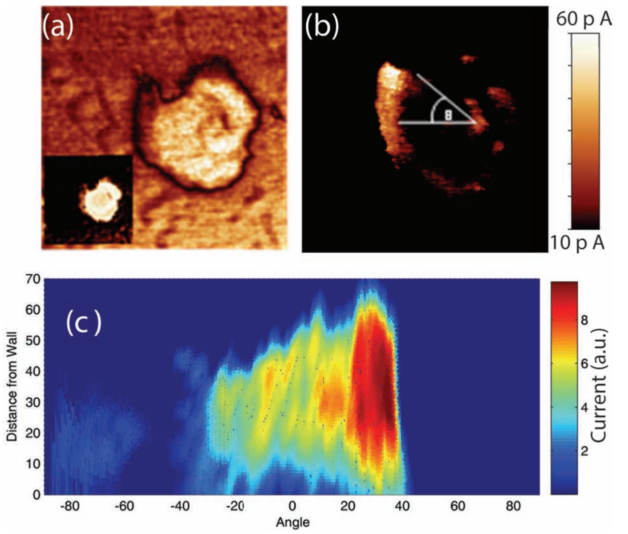

Figure 4. Conduction controlled by wall geometry. a) Vertical PFM Amplitude (phase inset) of domain structure. b) c-AFM in UHV, with V_{sample} = +2 V. The conduction around the left part of the wall was recalculated as a function of angle and distance from the wall, and is plotted in (c). Reproduced with permission.[96] Copyright 2012, American Chemical Society.

Naturally, the question remains as to whether such changes produce measurable alterations in conductivity that can be observed experimentally. It was reported[96] that these effects could indeed produce measurable changes in observable conductance. In **Figure 4**a,b, a PFM image and c-AFM image taken in UHV of a written circular domain structure is shown. The conduction data, plotted as a function of angle and distance from the domain wall, is shown in Figure 4c. Clearly, there exists significant variation in the current along the domain wall, due to wall geometry and associated charge distributions. These results indicate that spatial modulation of conduction in these thin films, through controlled writing of curved domain walls, is possible.

3.3. Hysteresis at Walls

The detailed studies of the domain wall conduction in the UHV environment additionally illustrate several remarkable aspects of this behavior.[20] Shown in **Figure 5**a is the piezoresponse image of the $BiFeO_3$ surface, demonstrating irregular domain walls. In comparison, shown are several conductive AFM images of the same region acquired sequentially in Figure 5b–d. While the general ferroelectric domain structure

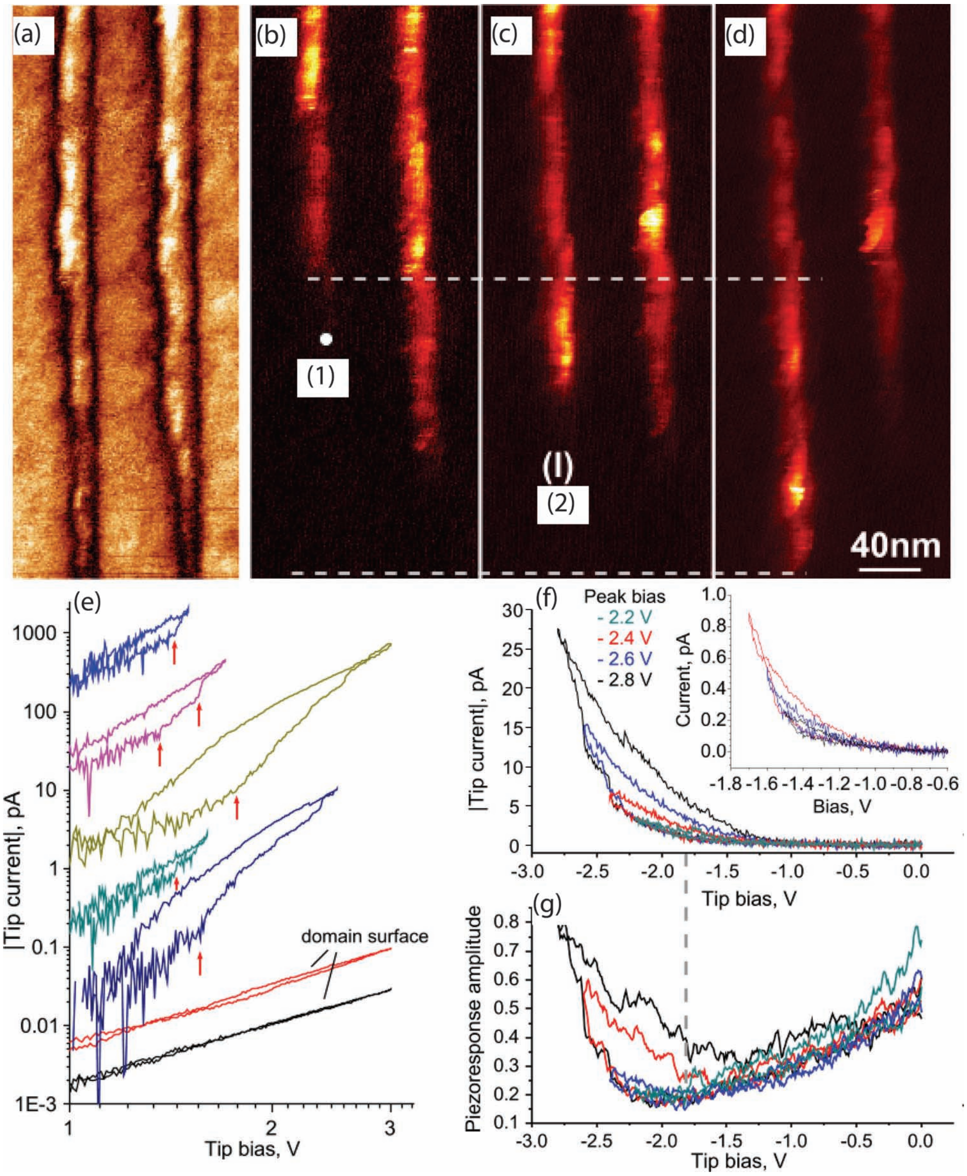

Figure 5. Dynamic conductivity of domain wall. a) Vertical PFM Amplitude image of 109° domain walls. b–d) A sequence of three current images of the domain walls obtained: b) before voltage stressing, c) after acquiring a series of *I–V* curves at location (1), and (C) after acquiring a similar series of *I–V* curves at the location marked in (2). The white dashed lines mark the region of the left domain wall the conduction of which was activated as a result of voltage stressing. e) *I–V* curves taken at four locations on the 109° domain walls and two on the domain surface. The red arrows indicate where the slope abruptly changes. f) *I–V* curves and concurrently obtained. g) Piezoresponse spectroscopy showing that the hysteresis in the *I–V* is accompanied with hysteresis in the piezoresponse, suggesting that polarization dynamics are the cause of the observed changes. Panels (a–e) are adapted with permission.[20] Copyright 2011, American Chemical Society.

remains the same, the conduction images show gradual increase of conduction along the wall. The wall is "activated" from the non-conductive to conductive state. Detailed examination of these images illustrates that conduction is uniform along the wall, but a number of "hot spots" can be observed. These regions of increased localized conduction can appear and disappear during the measurements, the behavior that can potentially be attributed to the interaction between the domain wall and extended defects in the film (e.g., compare with the electroresistive behavior of dislocations as observed by Szot et al.)[97,98]

This behavior is further illustrated in Figure 5e. Here, shown is the series of the *I–V* curves at dissimilar locations on the surface and in the vicinity of the wall. On the free surface, the curve is not hysteretic, suggesting the absence of slow polarization or ionic dynamics. At the same time, in the vicinity of the domain walls the curve exhibits the voltage activated increase in conductance. Note the relatively low conductance on the forward branch of the *I–V* curve, upturn to higher conductance level (marked by arrows). On reverse branch, the conductivity invariably stays at a higher level. Finally, the relationship between conductance and polarization behavior is illustrated in

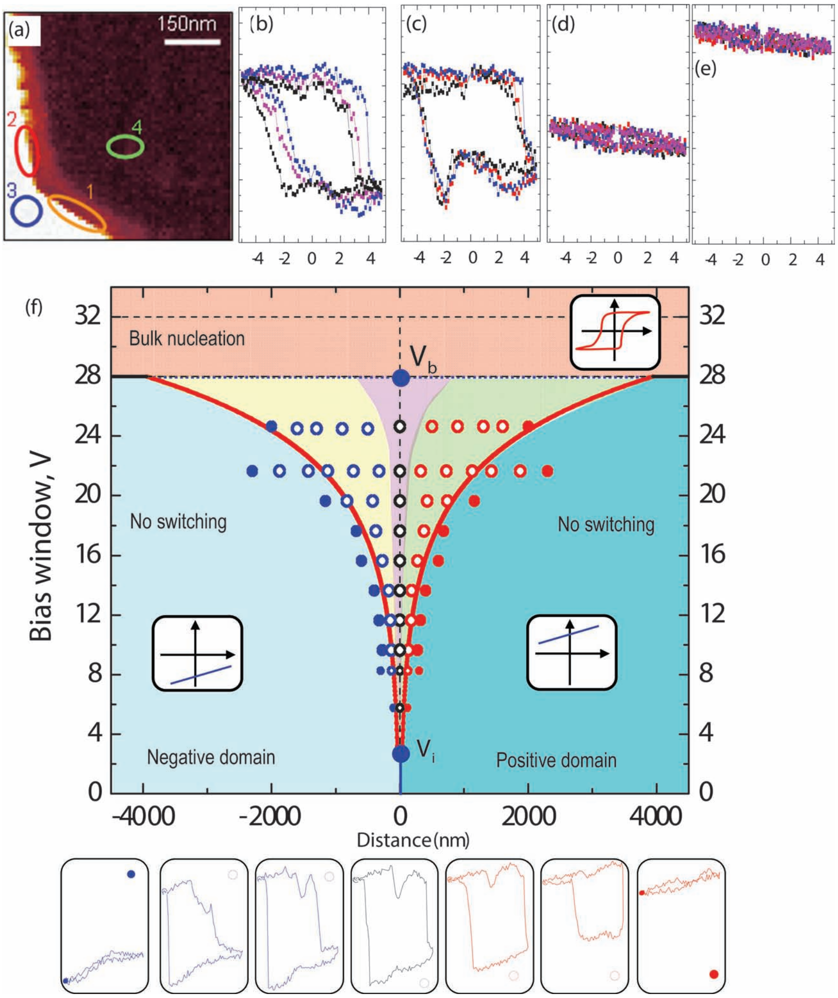

Figure 6. Influence of the domain wall on nucleation and switching. a) Piezoresponse after SS-PFM across a 180° domain wall in $LiNbO_3$. The bias-dependent piezoresponse loops for areas marked 1–4 are shown in (b-e).The loops away from the wall show no opening, while those in the vicinity of the wall show clear hysteresis. f) Dependence of loop shape on position from the domain wall and bias window. Reproduced with permission.[106] Copyright 2010, American Physical Society.

Figure 5f,g, showing the *I*–*V* curves acquired concurrently with the piezoresponse force spectroscopy. Note that hysteresis in the *I*–*V* behavior opens together with hysteresis in PFM signal, suggesting that the observed behavior is related with minute changes in polarization distributions (and wall geometry).

This behavior suggests that the domain wall can be displaced from its original position by the electric field of the tip, but the process is either reversible (i.e., wall relaxes to original location in the bias -off state) or the change is limited to a small location. While no specific studies of this behavior have been reported for BFO, this behavior agrees with existing models[99] and experimental studies[64,100,101] of single domain wall dynamics[102,103] in disordered media with quenched defects producing a randomly varying local potential.[104] In this context the wall can either move reversibly, implying oscillation within a single potential well, or irreversibly from overcoming the local potential barrier.[105] Locally, this behavior has been explored for domain walls in $LiNbO_3$ (LNO), providing the idealized macroscopic system.[106,107] Illustrated in **Figure 6** a is the piezoresponse across a domain wall in LNO, after Switching-Spectroscopy PFM experiment was carried out to gather the local switching properties. Hysteresis loops from selected areas in Figure 6a are shown in Figure 6b–e. The (off-field) hysteresis loops are open only at the domain wall and are closed away from it, indicative of local pinning dynamics. Remarkably, the wall positions changes only insignificantly during multiple switching cycles, suggesting the local stabilization by elastic forces from the unbiased wall segments or defect pinning. This behavior is highly bias dependent and the full diagram of wall behavior is illustrated in Figure 6f. This graphic highlights the critical role of the domain wall in the switching process, with the domain wall acting as a nucleation site at close distances, but also exerting influence up to ≈µm rages. In the vicinity of the domain wall, the voltage required to induce polarization switching reduces by an order of magnitude, while the imprint is minimal and the loops are largely symmetric. As the distance from the wall increases, imprint becomes more pronounced, and there is dramatic increase in the nucleation bias. The long-range influence of the domain wall on local switching is thought to be from local bending or bowing of the domain wall under applied field. A similar observation was reported in PZT thin films where the presence of a ferroelastic domain wall critically reduced the nucleation bias.[108]

This universality of domain wall dynamics, close link to the conductance, and capability to tune it locally suggests that the walls can be considered as a dynamic tunable conductor. Shown in **Figure 7**a is a periodic array of ferroelectric 109° domain walls in a $BiFeO_3$ film, which are conducting. The local I-V curves along the wall exhibit significant hysteresis, with current in the forward direction of the voltage sweep always lower than in the reverse direction. This behavior is more evident at the larger bias windows. Though the *I*–*V* curves are similar in the forward direction, they are pinched off at the maximum bias of the voltage cycle, yielding a unique reverse *I*–*V* curve each time. This behavior is reminiscent of memristive systems,[109] and in our case imply that the domain wall supports a quasi-continuous progression of distinct conducting states induced by electric field.

In order to decouple the change in conductance of the wall from the field-dependence of the conductivity, a special bias waveform consisting of 'read' and 'write' steps was employed, shown in Figure 7c, Cycling the waveform between 0 and –3.2 V tip bias revealed a hysteresis of conductance at –2.2 V, shown in Figure 7d with constant low and high conductance states and quasi-continuous transitions in between. Notably, the conductance

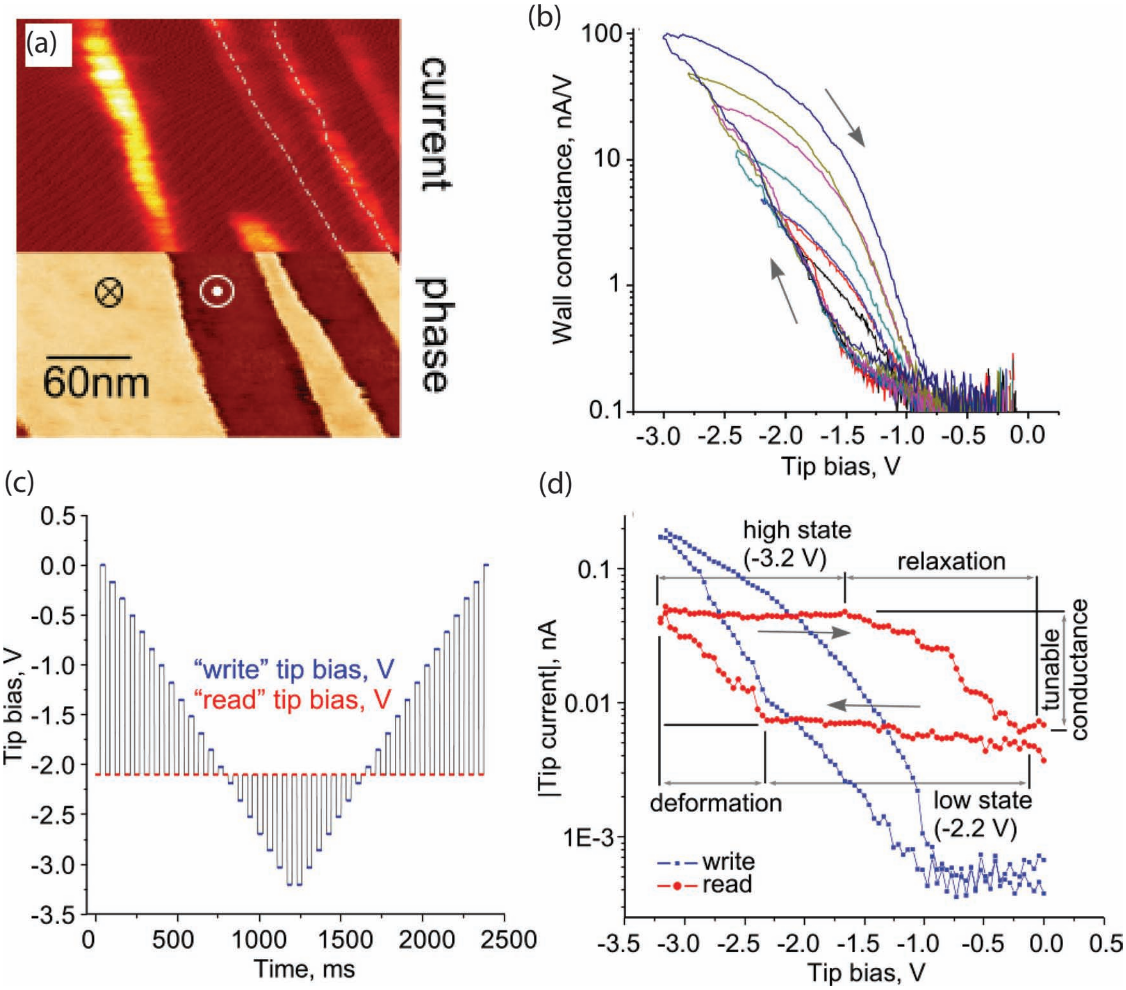

Figure 7. Variable resistance of a 109° domain wall in $BiFeO_3$. a) c-AFM and PFM Phase image of conducting domain walls. b) *I–V* Curves taken at a conducting domain wall with PFM phase and c-AFM image inset. To check the change in conductive state, the special waveform (c) was used. The result of this experiment is shown in (d) for both read and write states, and clearly indicates a memristive-type behavior of the domain walls. Adapted with permission.[20] Copyright 2011, American Chemical Society.

state created at –3.2 V was *stable* down to –1.7 V, and began to gradually relax between –1.7 V and 0 V. This can be seen clearly in the off-field hysteresis loop, plotted in red in Figure 7d.

These studies suggest that conductance behavior in ferroelectric domain walls is significantly more complex the simple static (constant resistance) conductor model considered previously. In particular, the walls exhibit many aspects of memristive systems as controlled by local polarization dynamics, including (1) electric-field induced topological distortion of the domain wall; (2) the dependence of conductivity on the degree of distortion; (3) weak-pinning of the distorted wall, manifested as the stability of the distorted configuration in a broad voltage-window. Hence, the domain wall offers a quasi-continuous spectrum of voltage-tunable electronic states, which is distinct from ferroelectric domains, where switching may give rise to discrete, and often only two conductance levels.[110] In total, the results suggest the slow kinetic processes of polarization dynamics or vacancy redistribution at the domain wall can significantly impact the measured conductivity, allow the possibility of tunable conductance, and further suggest that such conductivity could be ubiquitous in ferroics. However, domain walls which are strongly pinned (such as 90° ferroelastic domain walls in $Pb(Zr,Ti)O_3$, which are significantly clamped in thin films)[111] would not be expected to show conductivity arising from these mechanisms. Additionally, the possibility of sudden increases in the current (Barkhausen jumps),[112] associated with small but sudden displacements of the domain wall, would likely make the process unsuitable for device applications due to unpredictability.

4. Interface Modulated Conductance

4.1. Ferroelectric Tunneling

Whilst electron tunneling has been known since the initial development of quantum mechanics, material synthesis issues meant the idea of using a thin ferroelectric layer as the insulating barrier arose only relatively recently. The proposal for ferroelectric tunneling was originally based on the notion of the electronically insulating property of the ferroelectrics. Although this is generally true, common ferroelectrics such as titanates and bismuth ferrite are not very good band insulators with a gap of only 2.5–3.5 eV.[113,114] For SbSI, the band-gap is even smaller at ≈1.8eV.[115] Therefore, an alternative approach to polarization-controlled electron transport, not limited to ultrathin tunneling barriers, is to consider the coupling between semiconducting properties of bulk insulators and the topology of the order parameter either at the interface, or in the bulk volume. The former case is the ferroelectric Schottky diode that was demonstrated by Blom et al as early as in 1994. There, a 200 nm film of $PbTiO_3$ was sandwiched in a capacitor geometry between Au (top) and $La_{0.5}Sr_{0.5}CoO_3$ (bottom) electrodes, and the net “leakage” response of the capacitor was found to have transitions between different transport mechanisms associated with ferroelectric switching. The effect was interpreted in terms of the response of the space-charge distribution within the ferroelectric volume to the depolarizing field. The ferroelectric diode effect would correspond to the transition between the regimes of strong accumulation at the interface (a narrow Schottky barrier) and strong depletion (a wide barrier), yielding a large hysteresis in conductance. The concept of ferroelectric tunneling in oxides was introduced by Rodriguez-Contreras et al.,[116] who found that the resistance across a fabricated metal/PZT/metal junction could be switched between high and low states, and attributed the two resistance states to the two possible orientations of polarization in the ferroelectric film. The theoretical framework for this discovery of giant electroresistance was then developed by Tsymbal et al.,[110] who argued that the cause for the two states was the change in potential profile seen by the tunneling electrons, modulated by the dielectric polarization. Since then, many ferroelectric tunnel junctions have been experimentally realized,[117–120] and the concept has extended to use of multiferroic barriers (such as $BiFeO_3$), which allows an extra spin degree of freedom.[121,122] Further, recent work by Jiang et al.[123] has shown that resistance states can be reliable over several months, and with large on/off ratios, suggesting viability for commercial application.

Yet, earlier theoretical proposals have also hypothesized that inclined ferroelectric domain walls can themselves become conducting channels through the bulk volume of the material.[18] Though conceptually similar to the Schottky diode effect, the unscreened polarization charge, the respective depolarizing field and the ensuing localized volume of compensating carriers in this case exist within the bulk of the material, rather than its interfaces, potentially making the whole film conducting. This effect is the archetypal ferroelectric field effect acting at a homointerface, that, in our knowledge, predates the ideas of field effects at heterointerfaces (for example to control the T_c of the superconducting transition).[124]

Exploration of polarization-dependent electronic transport necessitates simultaneous measurements of both ferroelectric and conduction phenomena, similar to studies of domain walls in section 3. An example of polarization-controlled transport in the thick ferroelectric film is illustrated in **Figure 8**a, illustrating the current voltage curve and simultaneously acquired strain curve on a 30-nm-thick lead zirconate-titanate (PZT) film.[125] Note that the polarization switching event clearly identifiable by the jump in strain curve is simultaneous with the resistive switching event, suggesting the intricate link between the two. This behavior is further illustrated in Figure 8b, where switching proceeds through two steps both in *I–V* and piezoresponse data, and is confirmed over a large number of repeat experiments, as shown in Figure 8c. Finally, Figure 8d illustrates that in the absence of switching the *I–V* curve is smooth and no resistive switching is observed, thus unambiguously establishing the relationship between the two.

4.2. Memristive Behavior at the Nanodomains

Conducting domain walls offer an intriguing alternative to ferroelectric tunneling in thin films, because the net conductance only weakly depends on the film thickness (or not at all) allowing much thicker ferroelectric films to be used for resistive switching and other conductance-related phenomena, and providing potentially much larger current densities. Furthermore, the sign and density of the compensating carriers will depend on the sign and density of the bound polarization charge, respectively, and the domain wall can therefore potentially be used to completely control bipolar transport through the same region of the material (provided enough compensating carriers exist).

We have recently explored the basic principles of this type of conduction phenomenon to modulate the conduction in ferroelectric nanodomains in a 50 nm PZT film.[87] The current enhancement is very pronounced in the data in **Figure 9**a, where a region with negative resistance immediately after switching event is seen. Comparison of this data with the data on domain wall conductance leads to an assumption that it is the ferroelectric nanodomain formed during switching event that acts as a conductive channel, rather than modification of Schottky barrier directly below the tip.

Such an interpretation is supported by Figure 9b, exploring the conductance behavior in a series of first-order reversal curves. Note the evolution of conductivity with the bias history, indicative of the expansion and contraction of nanodomain below the probe. This memristive-type behavior allows the opportunity to tune the conductance of nanodomain by altering its size, and is illustrated in Figure 9c,d.

4.3. Metallic Conductivity

The temperature-dependent conduction properties of written nanodomains has been explored, with results shown in **Figure 10**. Interestingly, whilst the domain walls and the macrodomain are governed by thermally-activated conduction with an activation energy of 200–250 meV, the conductivity of the written nanodomains show almost no temperature dependence, across voltage ranges up to 9 V. Such behavior rules out hopping conduction mechanism, which has been observed for PZT,[41] and suggests a fundamentally different transport regime in the nanodomains.

There are two possible mechanisms for negligibly temperature-dependent conduction: electron tunneling and metallic

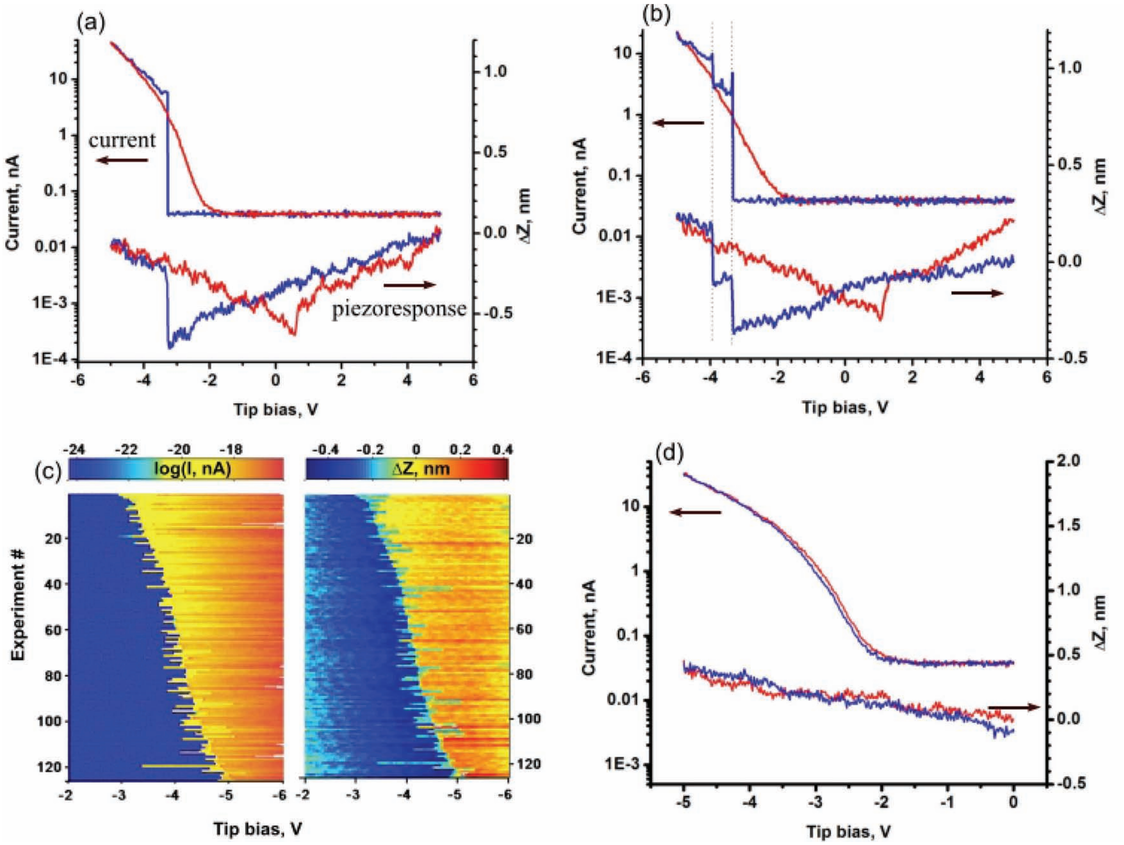

Figure 8. Simultaneous measurements of local piezoresponse and conductance on the surface of a 30 nm PZT film. a,b) *I–V* curves and strain curves for voltage range –5 to 5 V. c) Correlation between current and strain curves based on 126 measurements acquired on a 6400 nm^2 grid with a lateral resolution of 20 nm. Each horizontal line in the images corresponds to one forward *I–V* (left) and its matching strain (right) curve. Both *I–V* and strain curves in the data set were sorted according to the negative tip bias at current discontinuity. The discontinuities lie along the boundary of the blue and yellow regions. The boundaries are identical in the current and strain measurements, revealing the perfect correlation between the respective discontinuities. Streaks in the images correspond to the *I–V*/strain curves with double jumps as in (b). (d) *I–V* curves for 0 to –5 V were also captured, illustrating smooth monotonic behavior in the absence of polarization switching. Reproduced with permission.[125] Copyright 2009, AAAS.

conductivity. Though the *I–V* curves for the nanodomains show an exponential shape, as in Figure 9a, suggestive of Fowler–Nordheim tunneling, [126] the studied film is much too thick for tunneling across the whole film. Therefore the bulk of the film in the nanodomain must be conducting to a much greater extent than the macrodomain, and further the conduction mechanism must be very weakly (or not at all) temperature dependent.

Overall, this data establishes a conclusive connection between polarization hysteresis and resistive switching in moderately thick films of PZT and BFO (in the range of 5–100 nm). Notably, Kohlstedt et al.[127]emphasized that only when ferroelectric switching is synchronized in voltage with resistive switching, the two values can be deemed connected. We have extended this criterion by demonstrating also that when no ferroelectric hysteresis was observed in a considerably large range of applied tip voltage (from –5 V to + 1 V), no resistive switching occurs, and the transition between net non-hysteretic and net hysteretic electron transport was triggered by the minimum voltage required to reverse spontaneous polarization. Local microscopy techniques can therefore efficiently probe both net transport through the film, which can be considered a rigid dielectric in a special case (or mixed electron-ionic conductor in a more general case), and transport events caused by the changes in polarization topology. This last regime is typically concealed in macroscopic capacitor measurements by the large peak of the displacement current.

The actual manifestation of the ferroelectric switching in the thick PZT film was a dramatic increase of local conductance when the polarization of the monodomain downward-polarized film is locally switched to the upward polarization, as shown in the data and schematics in Figure 10b. The *I–V* curves of the conducting upward polarized domains were highly rectifying, and were interpreted in terms of the Fowler-Nordheim tunneling mechanism. Its polarization dependence would be largely consistent with the ideas of the ferroelectric Schottky diode, and, in fact, Schottky emission could also be potentially the transport mechanism provided the limiting interfacial barrier would be small enough. A number of puzzling details could not, however, be explained within the canonical picture of bistable conductance and interfacial tunneling mechanisms: (1) why are the *I–V* curves so highly rectifying, with no measurable

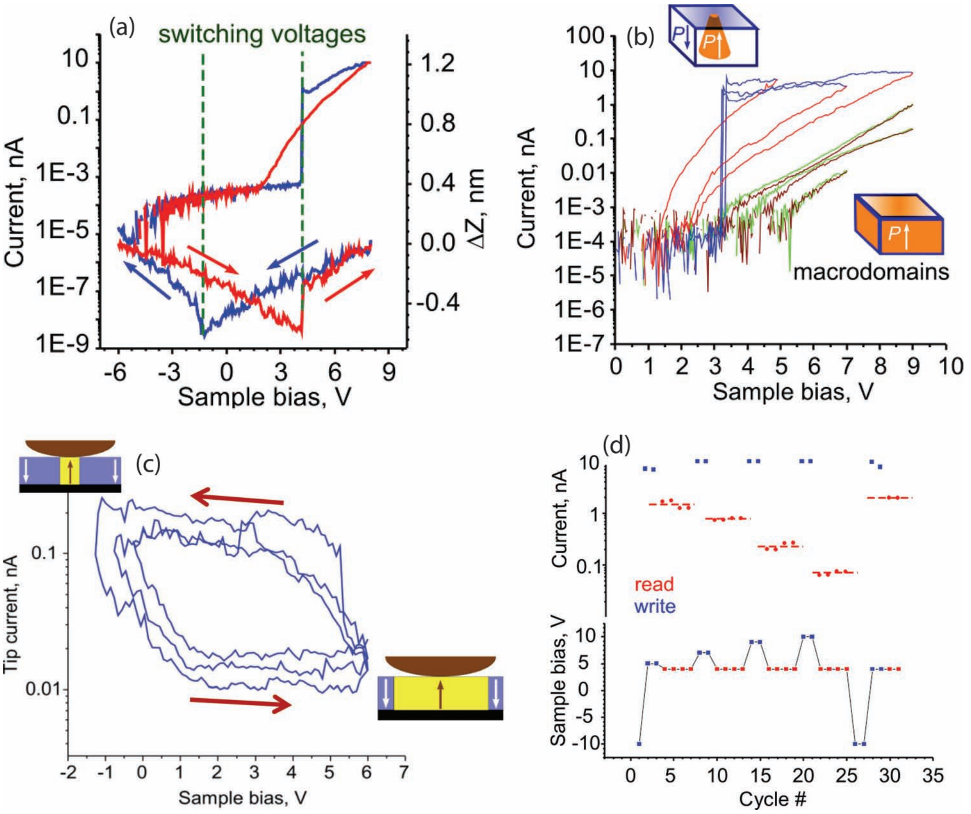

Figure 9. Conductivity of ferroelectric nanodomains. a) Simultaneous *I–V* and piezoresponse (strain) curves. b) *I–V* curves (only positive voltages shown) for nano- (red, blue) and macro- (brown, green) domains. c) Hysteresis in conduction. This offers the ability to tune the conduction over many cycles by writing pulses of different voltages, as shown in (d). Adapted with permission.[87] Copyright 2012, American Chemical Society.

current at positive tip bias (in the probed range); (2) why is the absolute current relatively large, in the 10–100 nA range; (3) what is the origin of mild secondary hysteresis around the polarization events. The answers to some of these questions were found by a detailed comparison of the local conductance of different ferroelectric topologies created by the AFM tip, shown in Figure 10c. Specifically, we compared: (1) *I–V* curves obtained on the surface of a upward-polarized nanoscale domain created right under the tip at the instance of polarization switching; (2) *I–V* curves on the surface of the upward-polarized macroscopic domain with the linear dimension exceeding 100 nm, that was created by poling the surface with an appropriately biased tip and (3) finite conductivity of ferroelectric domain walls decorating macroscopic domains, that turned out to be also conducting in direct analogy to conductive domain walls in multiferroic $BiFeO_3$[19] and consistent with the measurements on the PZT film of similar composition.[41]

Of the three conductors, the nanodomain was special because it was not only the most conducting entity on the PZT surface (by orders of magnitude), but also because the nanodomain conductance was negligibly temperature-dependent between 100 and 300 K, irrespectively of the probing bias (at least up to 9 V), forward or reverse branch or even the measurement protocol used to acquire the *I–V* curve. At the same time, both the conductance of macroscopic domain walls and the surfaces of macroscopic domains were governed by thermally-activated conduction. In light of this evidence, the nanodomains were surmised to be net metallic conductors, in contrast to the net insulating property of the other two entities. More generally, this observation makes the interpretation of both electron transport mechanism and its polarization dependence a complicated and strongly coupled problem, because both interface and bulk regions now have to be considered. Yet, surprisingly, metallic domain walls can account for the above observations, if only qualitatively at first. Indeed, the activation of a conduction channel through the bulk of the material can explain the large currents observed in relatively thick 30–100 nm films. A secondary hysteresis of the *I–V* curves after polarization switching is directly related to the size of the nanodomains, and most likely to the tilt of the domain walls. Additionally the secondary hysteresis confirms the theoretical prediction of the tunable degree of conductance of the domain wall. As to the strongly rectifying character of the *I–V* curves, there are two possible explanations: (1) carrier compensation of the domain wall occurs by carriers of only one sign (in our case electrons); (2) the domain nucleation/growth mechanisms are not symmetric in bias. The second scenario occurs in PZT, wherein the upward polarization domain collapses when subjected to positive tip bias, as opposed to its annihilation with a newly-nucleated downward-polarized domain. In this case, there exist no domain walls after polarization reversal to the downward-polarized state and film remains a net insulator.

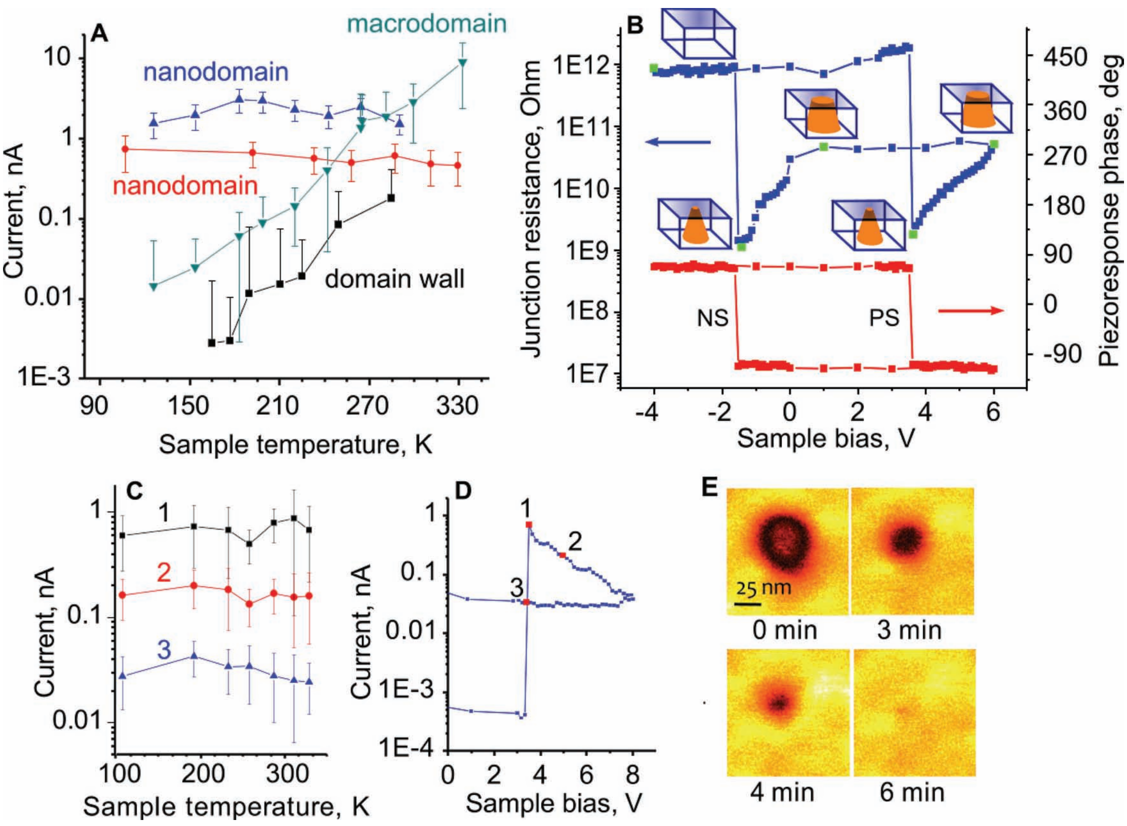

Figure 10. Temperature dependence of conduction. a) Temperature-dependence of local current obtained from averages of ≈100 hysteretic *I–V* curves on nanodomains (blue, measured at 4.5 V), ≈ 50 resistive curves on nanodomains (red, measured at 3.5 V), ≈ 100 non-hysteretic *I–V* curves on macrodomains (green, measured at 7 V) and one c-AFM image from the domain walls (measured at 2.6 V) at each temperature. Error bars are standard deviation for each data set. b) Top: resistance of the tip-surface junction at sample bias of 2.6 V. Cartoon schematics show nanodomains of upward polarized nanodomain (orange) believed to be formed at various instances of the resistance curve (green points). Bottom: phase of local piezoresponse accompanying the resistance curve. PS and NS mark the positive and negative switching events, respectively, as judged from a phase flip by 180°. c) Temperature-dependence of the tunable conductivity of nanodomains as a function of their size, black–smallest (at creation), red - intermediate and blue–average equilibrium size at sample bias of 8 V. d) One of ≈50 resistance curves at $T = 329$ K, showing the positions (domain sizes) sampled in (c). e) Piezoresponse amplitude images of a nanodomain, as a function of time. The nanodomain spontaneously disappears after ≈6 min due to a strong built-in electric field. Adapted with permission.[87] Copyright 2012, American Chemical Society.

Finally, tunable conduction of the domain walls allows one to make a transition from a binary memory-like functionality of polarization-controlled transport in ferroelectrics to a more general case of memristive behavior. A simple demonstration that there exists almost a continuum of resistive states tunable by voltage is shown in Figure 9d. Here, the appropriate nanodomain is created at cycle 0, and its size is subsequently manipulated by the negative voltage of varying magnitude, but without erasing it. Tunable conductance states can therefore be achieved by the size-control of the nanodomain, which requires significantly smaller operating voltages and voltage thresholds than polarization reversal, and could potentially be less prone to fatigue. The resistance variation can be well over two-orders of magnitude, and it can have both positive and negative voltage slope. Recently, a complementary way to achieve memristance in a ferroelectric tunnel junction was reported, where the area of appropriately oriented domains, rather than the size of a single domain (or the tilt of its wall) was the physical state variable.[15] Potentially, the two approaches can be joined to create a very flexible architecture for memristive effects.

Overall, the control of transport in thick ferroelectric films is a direction that complements tunnel junctions. These developing areas highlight the richness of polarization-coupled transport phenomena even in conventional ferroelectric materials. We anticipate that their extension onto thin films and atomically-precise oxide superlattices of multiferroics, mixed-phase and anti-ferroelectrics will reveal a whole family of previously unknown electronic properties of these materials, paving way to new fundamental and applied prospects of oxide nanoelectronics.

5. Conduction of Domains and Charged Domain Walls in Hexagonal Manganites

Charged ferroelectric domain walls, which may host novel conduction properties, are rarely observed in conventional ferroelectrics due to unfavorable energetics. Recently, it has been revealed that numerous charged domain walls are presented in hexagonal manganites due to formation of 6-state vortex network, and they do possess different conduction properties besides the Schottky-like conduction. Herein, we review the observation of polarization-modulated rectification along the ferroelectric polarization direction and the discovery of nanoscale conduction of the fascinating charged domain walls perpendicular to the ferroelectric polarization direction using in situ scanning probe microscopy in the Center for Nanoscale Materials at Argonne National Laboratory.

5.1. Introduction and Motivation

The coupled order parameters in multiferroics–where magnetism and ferroelectricity coexist[128,129]–provide an interesting playground for topological defects, which are pervasive in complex systems such as superfluids, liquid crystals, and the early universe.[130,131] Recently a new kind of topological defect with six interlocked structural antiphase and ferroelectric domain walls merging into a vortex core was discovered in hexagonal (*h*-) manganite $YMnO_3$.[132,133] *h-RE* MnO_3 (*RE* = Sc, Y, Ho, … Lu) are multiferroics with coexistence of ferroelectricity ($T_C \approx$ 1200–1500 K) and antiferromagnetism ($T_N \approx$ 70–120 K).[134,135] The ferroelectricity in *h-RE* MnO_3 is a by-product of primary structural instability called trimerization.[136,137] Therefore, *h-RE* MnO_3 are improper ferroelectrics where polarization plays no role in the formation of the vortex-antivortex network near T_X. In other words, the formation of topological vortex-antivortex pairs and highly-curved vortex cores is thermodynamically favorable because of the entropic contribution to the free energy.[130] Note that earlier imaging studies of ferroelectric domain structure by Safrankova et al[138] could not identify the topological vortex domain structure because of poor spatial resolution, though their observation of irregular domain structure is consistent with recent studies. Here we use "topological vortex" to emphasize the topological nature of the defect lines in *h-RE* MnO_3, which are a discrete version of vortices in superfluids and superconductors.

The band gap of *h-RE* MnO_3 is relatively small (≈1.7 eV),[139] so the charge transport properties of ferroelectric domains and topological vortices may show interesting emergent behavior. Indeed, the ferroelectric polarization in *h*-$REMnO_3$ does influence the Schottky-like barriers (and therefore, the conduction) of domains on the polar (001) surface of *h*-$REMnO_3$ as discussed below.[132,140] Schottky injection has been considered as a source of electric leakage which is detrimental to ferroelectric applications.[141] The polarization modulated Schottky-like conduction observed in *h*-$REMnO_3$ opens new possibilities of high resolution imaging of ferroelectric domain[3] states and non-destructive readout method for ferroelectric memory devices.

In addition to the interesting conduction modulation on polar surface, numerous "charged ferroelectric domain walls"—where opposite polarizations are facing to each other[133,142,143]—arise naturally from the topology of vortex-antivortex network in a 3D crystal. Previous studies in conventional ferroelectrics have focused on neutral domain walls; charged domain walls, which are rarely observed due to unfavorable electrostatic and/or strain energy cost, are often associated with defects or needle-shape domains during polarization reversal.[21,23,144–149] In contrast, the charged domain walls in multiferroic *h-RE* MnO_3 are intrinsic to the topology because of the presence of highly curved topological vortex cores.[133,142,143] Therefore, the family of *h*-RE MnO_3 provides a unique model system to study conduction properties of charged domain walls that are rarely observed in conventional ferroelectrics.[90,91]

5.2. Experimental Methods

In this section, we focus on single crystals of *h*-$HoMnO_3$ were grown by using the floating zone method. The (001) surface was prepared by mechanical polishing and annealing to 875 K to reduce polishing strain (roughness ≈ 3 nm), while the atomically flat (110) surface was obtained by mechanically cleaving in ambient conditions. The *c*-axis orientation was determined by Laué X-ray backscattering. In either orientation, the sample was glued to a sapphire substrate with a Ag epoxy, which also served as the back electrode. Scanning probe measurements were performed with a commercial ultrahigh vacuum (UHV) variable temperature (VT) atomic force microscope (AFM) (Omicron). cAFM and PFM were performed in contact mode with the conductive AFM tip (either Au or Pt/Ir coated cantilevers) as the top electrode. Kelvin-probe force microscopy (KPFM) was performed in tapping mode with the bias modulated at 20–100 kHz. Electrostatic force microscopy (EFM) was performed in noncontact mode with cantilever operating at its resonant frequency.

5.3. Polarization-Modulated Rectification of Ferroelectric Domains on Polar Surface

Schottky barriers form at the interface between a metal and a semiconductor due to the mismatch of work functions between them. The resulting charge redistribution across the interface leads to asymmetric charge transport through the interface and rectification in the *I*–*V* curves. Since ferroelectrics are also semiconductors, Schottky-like conduction is often observed. In contrast to non-polar semiconductors, the polar surface of ferroelectric (due to termination of polarization) influences the charge redistribution and the barrier height and, therefore, the rectification. Such effect has been widely observed in micrometer-sized ferroelectric devices.

Using a combination of SPM techniques, the polarization-modulated rectification on the (001) manganite surface can be explored directly by correlating local IV properties with the ferroelectric domains. The domains can be imaged directly by mapping the local electrostatic interaction (superposed on the attractive van der Waals interaction) between the sample and the tip with EFM. **Figure 11**a shows an EFM image at a temperature (141 K) where the charges are frozen out and the polarization can be seen. With negative tip bias (−3 V), bright (dark) contrast in the EFM images indicates stronger (weaker) attractive interactions due to positive (negative) surface charges, indicating domains with polarization pointing up (down). Figure 11b shows the cAFM map of the same region of the $HoMnO_3$ (001) surface at room temperature. Comparing this conduction map (V_{tip} = −6 V) to the EFM map, clear correlations are observed: the up domains identified by EFM show a larger conduction than the down domains.

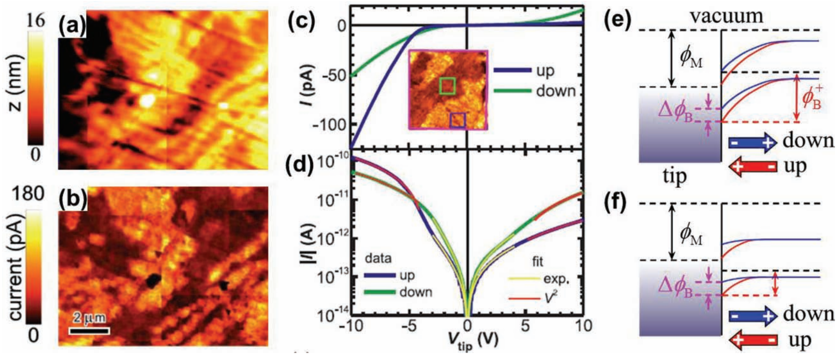

Figure 11. Conduction of polar (001) surface in $HoMnO_3$. a) EFM (141 K) and b) cAFM (300 K) map of the same region of the $HoMnO_3$(001) surface. c) Linear and d) semilog plots of spatially averaged I–V curves from up (blue) and down (green) domains as indicated on the cAFM image in the inset ($V_{tip} = -6$ V). Interfacial schematic band diagrams between cAFM tip and FE domains for (e) $V_{tip} > 0$ (reverse bias) and (f) $V_{tip} < 0$ (forward bias). Reproduced with permission.[140] Copyright 2010, American Physical Society.

This spatial contrast arises due to differences in the I–V characteristics of the domains; Figure 11c,d show I–V curves averaged over up (blue) and down (green) domains (as indicated in the inset). At low bias ($|V_{tip}| < 3$ V), the I–V curves in both domains are dominated by the Schottky barrier at the metal-semiconductor interface. The forward bias direction corresponds to $V_{tip} < 0$ as expected for p-type $HoMnO_3$;[141,150] as indicated in the interfacial band diagrams shown in Figure 11e,f, the Schottky barrier increases with larger reverse bias ($V_{tip} > 0$) and decreases with larger forward bias ($V_{tip} < 0$), leading to rectification. However, this rectification is modified by the local polarization of the ferroelectric domain. The band-bending associated with the work function mismatch between the metal tip and the p-type $HoMnO_3$ is expected to be enhanced (suppressed) by the surface charge on the up (down) domains, leading to a larger (smaller) Schottky-like barrier. The lower barrier in the down domains leads to a larger current in the $|V_{tip}| < 3$ V regime, as observed in Figure 11b. The exponential nature of the Schottky-like transport can be seen in the exponential fits in Figure 11d. At higher forward and reverse bias ($|V_{tip}| > 5$ V), the charge transport appears to be in the space-charge limited conduction (SCLC) regime and can be described by Child's law as seen by the $I \propto V^2$ fit in the figure.[141]

5.4. Conduction of Charged Domain Walls on Non-Polar Surface

For the non-polar (110) surface of h-$REMnO_3$, in-plane PFM at room temperature can identify vortices along the c- axis[142,143] as shown in **Figure 12**(b). The cantilever was parallel to the c-axis, therefore, the PFM signal (vertical deflection) originates from the buckling of the cantilever.[143,151] The dark and bright contrasts represent in-plane up and down ferroelectric domains, which were determined by the phase of the PFM signal and confirmed by KPFM measurements at 65 K.[90]

As discussed above, c-AFM studies on the (001) surface of h-$HoMnO_3$ reveal non-linear I–V characteristics due to a Schottky-like barrier between the tip (a metal) and crystal (a p-type semiconductor).[152] On the (110) surface of $HoMnO_3$, the ferroelectric polarization is parallel to the surface and no difference in conduction is expected between opposite domains. This is confirmed experimentally through the lack of current contrast between opposite polarization domains in the c-AFM images in Figure 12a,c. These two c-AFM images show that the tail-to-tail domain walls are more conductive at both forward and reverse biases, while head-to-head domain walls are less conductive at reverse bias. This observation is consistent with recent theories that charged 180° domain walls in ferroelectric semiconductors attract (repel) mobile charge carriers with the opposite (same) sign.[153,154] For h-$HoMnO_3$, the conduction of tail-to-tail domain walls (which attract holes) is enhanced, while that of head-to-head domain walls (which repel holes) is reduced. This scenario, shown schematically in the band diagrams in Figure 12d, is qualitatively consistent with our observation. These intriguing conduction properties of 180° charged domain walls has been confirmed in multiple locations of our single crystal h-$HoMnO_3$ using various AFM cantilevers with different conductive coating materials,[90] as well as in h-$ErMnO_3$ by Meier et al.,[91] suggesting that they are intrinsic properties of h- $REMnO_3$. The widths of head-to-head domain walls (≈120–250 nm) are larger than that of tail-to-tail domain walls (≈80–100 nm), suggesting larger screening length at positively charged domain walls. This is because head-to-head domain walls repel holes and generate a space charge region which increases the domain wall width.[23] Note that the observed width of tail-to-tail domain walls may be limited by the cAFM tip radius (≤50 nm). The intrinsic conducting domain wall width could be much smaller than 10 nm.[23]

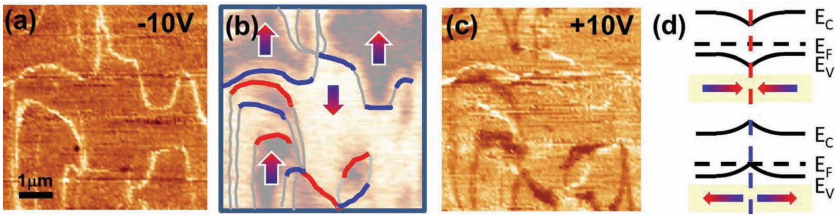

Figure 12. c-AFM of domain walls on non-polar (110) surface in $HoMnO_3$. a) c-AFM with forward bias (−10 V), b) PFM ($V_{ex} = 22$ V, $f = 21$ kHz) and c) cAFM with reverse bias (+10 V) images taken at 300 K. The PFM image is overlaid by a cartoon sketch of ferroelectric domain walls. Red, blue, and grey lines represent head-to-head, tail-to-tail and neutral domain walls, respectively. The arrows indicate in-plane polarization orientation determined from the phase of PFM signal. d) Schematic diagrams of band bending near charged domain walls. Upper panel: head-to-head domain walls, lower panel: tail-to-tail domain walls. Reproduced with permission.[90] Copyright 2012, American Physical Society.

Transport of charge carriers confined at interfaces or surfaces is an intriguing area in condensed matter physics to search for emergent phenomena, examples of which include the quantum hall effect at GaAs/AlGaAs with modulation doping,[155] tunable superconductivity at $LaAlO_3$/$SrTiO_3$ with charge catastrophe[156] and multiferroic tunneling junction at the $BaTiO_3$/Fe interface.[157] However, many of these interfaces and surfaces are limited by defects due to intrinsic imperfection in the fabrication process which can lead to detrimental scattering of charge carriers. In multiferroic *h-RE* MnO_3, charged ferroelectric domain walls are protected by the presence of topological defects in the form of vortices, which opens up opportunities for a new kind of nanoscale conduction channel in multifunctional devices. Charged ferroelectric domain walls may provide a platform for correlated 2-dimensional electron gas without utilizing chemical doping.

6. LGD Theory of Domain Wall Conduction

In this section, we discuss recent theoretical advances in the field. Landau-Ginzburg-Devonshire (LGD) formalism is introduced to explain the conductivity in uniaxial and multiaxial ferroelectrics at charged domain walls. The theory is then extended to explain the origins of conductivity in nominally uncharged domain walls, which is shown to arise from changes in the band structure across the domain wall in agreement with first-principles theory.[158] The origins of anisotropic conduction in both charged and uncharged systems is explored, and finally the theory of conduction in hexagonal manganites, which have recently been the focus of experimental studies,[90,91] is discussed.

Domain walls conductivity in ferroelectrics-semiconductors stem from the screening of depolarization field by free carriers.[18,159] LGD theory has proven to be a powerful tool for modeling domain walls' polar structure and electronic properties in uniaxial,[21,23] multiaxial ferroelectrics,[24,25,85,160–163] and incipient ferroelectrics–ferroelastics.[85]

Most of the reported works do not consider the impact of the flexoelectric coupling on domain wall structure, energy and electronic properties. The flexoelectric effect describes the coupling of polarization with strain gradient and polarization gradient with the strain.[164–166] Studies of flexoelectricity-related strong electromechanical coupling at the nanoscale in conventional[167–172] and incipient[173] ferroelectrics, have been performed with the LGD approach and confirmed by experimental trends.[174,175] Yudin et al.[176] showed that the flexoelectric coupling induces a Bloch-type polarization component with a structure qualitatively different from the classical Bloch-wall structure in tetragonal $BaTiO_3$. As such, the flexoelectric effect is thus important to include in LGD studies.

6.1. LGD Theory Formalism

Let us consider 180° domain wall in the bulk of ferroelectric. Within LGD theory, equations of state for polarization components and elastic stresses can be derived from the minimization of the Gibbs potential, which density for the *m3m* parent (paraelectric) symmetry has the form:[24,25,163]

$$G = G_{polar} + G_{grad} + G_{striction} + G_{elastic} + G_{flexoelectric} + G_{dep} \tag{1}$$

Here, $G_{polar} = a_i\ P^2{}_i + a_{ij}\ P^2{}_i\ P^2{}_j + a_{ijk}\ P^2{}_i\ P^2{}_j\ P_k{}^2$ is the Landau term, $G_{grad} = \frac{g_{ijkl}}{2}\frac{\partial P_i}{\partial x_j}\frac{\partial P_k}{\partial x_l}$ is gradient or Ginsburg term, $G_{striction} = -Q_{ijkl}\ \sigma_{ij}\ P_k P_l$ is electrostriction term, $G_{elastic} = -\frac{s_{ijkl}}{2}\sigma_{ij}\sigma_{kl}$ is elastic contribution, $G_{flexoelectric} = \frac{F_{ijkl}}{2}\left(\sigma_{ij}\frac{\partial P_k}{\partial x_l} - P_k\frac{\partial \sigma_{ij}}{\partial x_l}\right)$ is flexoelectric contribution, and $G_{dep} = -P_i E_i^d/2$ is the contribution of depolarization field.

Here after a_i, a_{ij} and a_{ijk} are LGD-expansion coefficients of the 2nd, 4th, and 6th order dielectric stiffness tensors correspondingly, gradient coefficients are g_{ijkl}, Q_{ijkl} are 4-th second rank electrostriction tensors coefficients, and zs_{ijkl} are elastic compliances included in the different terms in equation (1). $E_k = -\partial\varphi/\partial x_k$ are the components of depolarization electric field, ϕ is the electric field potential. Electrostatic potential ϕ should be determined from the Poisson equation,

$$\varepsilon_0\varepsilon_b\frac{\partial^2\varphi}{\partial x_i^2} = \frac{\partial P_i}{\partial x_i} - \rho \tag{2}$$

where ε_b is background permittivity[177] and $\varepsilon_0 = 8.85 \times 10^{-12}$ F/m is the dielectric constant of vacuum. The space charge density in equation (2) is $\rho = e\ (N^+{}_d - N_a{}^- + p - n)$, where $e = 1.6 \times 10^{-19}$ C is the electron charge, n is the electron density in the conduction band; p is hole density in the valence band; $N^+{}_d$ and $N^-{}_a$ are the concentrations of ionized shallow donors and acceptors correspondingly. The charges are in the units of electron charge $e = 1.6 \times 10^{-19}$ C, $\varepsilon_0 = 8.85 \times 10^{-12}$ F/m is the universal dielectric constant, ε_{11} is dielectric permittivity in the direction normal to the polar axis, $\varepsilon^b{}_{33}$ is the background. Ionized deep acceptors with field-independent concentration $N^-{}_a$ play the role of a background charge. If the donor level can be regarded infinitely thin with activation energy E_d, the concentration of ionized donors is determined by a Fermi–Dirac distribution function $N^+{}_d\ (\phi) = N_{d0}(1 - f\ (E_d - E_F - e\ \phi))$, where N_{d0} is the concentration of donors. The concentration of free electrons and holes included in the space charge density ρ in equation (2) in the continuous levels approximation[23] are:

$$p\,(\varphi) = \int_0^\infty d\varepsilon \cdot g_p\,(\varepsilon)\,f\,(\varepsilon - E_V + E_F + e\varphi) \tag{3}$$

$$n\,(\varphi) = \int_0^\infty d\varepsilon \cdot g_n\,(\varepsilon)\,f\,(\varepsilon + E_C - E_F - e\varphi) \tag{4}$$

where $f\,(x) = (1 + \exp\,(x/k_B T))^{-1}$ is the Fermi–Dirac distribution function, $k_B = 1.3807 \times 10^{-23}$ J/K, T is the absolute temperature. E_F is the Fermi energy level, E_d is the donor level, E_C is the bottom of conductive band, E_V is the top of the valence band. In the effective mass approximation densities of states are $g_n\,(\varepsilon) \approx \frac{\sqrt{2m_n^3\varepsilon}}{2\pi^2\hbar^3}$ and $g_p\,(\varepsilon) \approx \frac{\sqrt{2m_p^3\varepsilon}}{2\pi^2\hbar^3}$.

Donor (or acceptors) impact to the charge density can be neglected, since ion mobility (if any) is much smaller than the electron one. Hence, the relative charge density (related to local conductivity, and hence cAFM contrast) can be estimated as:

$$\frac{\sigma}{\sigma_{bulk}} = \frac{e\left(\eta_e n + \eta_p p\right)}{e\left(\eta_e n_{bulk} + \eta_p p_{bulk}\right)} \approx \frac{n}{n_{bulk}} \tag{5}$$

Since usually $m_n < < m_p$ (and therefore the mobility $\eta_e > > \eta_p$) the most pronounced is the static electronic conductivity.

Electrons and holes densities in Equation (5) are given by Equations (3, 4) possibly including the coupling between the inhomogeneous strain and band structure due to the deformation potential.[178] The strain-induced conduction and valence band edge shift caused by the domain wall is linearly proportional to the strain variation δu_{ij}:[25,85]

$$E_C = E_{C0} + \Xi^C_{ij}\delta u_{ij}, \quad E_V = E_{V0} + \Xi^V_{ij}\delta u_{ij} \tag{6}$$

where $\Xi^{C,V}{}_{ij}$ is a tensor deformation potential of electrons in the conduction (C) or valence (V) bands. Values E_{C0} and E_{V0} already includes the spontaneous strain $u^S{}_{ij} = Q_{ijkl}P^S{}_k\ P_l\ S$ existing far from the domain wall. Allowing for the possible strain-dependence of the Fermi level,[179] "effective" deformation potentials are used in Equation (6). It is worth to underline that a continuous band structure can be absent across the domain wall of thickness $r_c \approx 1$ nm, since quantization should exist in the direction transverse to the wall plane. However the potential barrier or well calculated within continuum LGD theory can be included into the quantum-mechanical treatment.

Regarding that all physical quantities can depend only on the distance $\tilde{x}$ from the domain wall plane $\tilde{x} = 0$, it makes sense to define them in the coordinate frame $\{\tilde{x}, \tilde{y}, \tilde{z}\}$ rotated with respect to the pseudo-cubic crystallographic axes $\{x_1, x_2, x_3\}$ in appropriate way.[23–25,160,161]

Euler-Lagrange equations[180] for polarization components were derived from the minimization of the Gibbs potential as $\partial\tilde{G}/\partial\tilde{P}_i - \partial\left(\partial\tilde{G}/\partial\left(\partial\tilde{P}_i/\partial\tilde{x}\right)\right)/\tilde{x} = 0$. Equations of state for elastic stresses are $\partial\tilde{G}/\partial\tilde{\sigma}_{ij} = -\tilde{u}_{ij}$, where $\tilde{u}_{ij}$ are elastic strains. They were solved along with mechanical equilibrium conditions $\partial\tilde{\sigma}_{1j}/\partial\tilde{x} = 0$, compatibility relations and boundary condition of the stress vanishing far from the wall, $\tilde{\sigma}_{ij}(\tilde{x} \to \pm\infty) = 0$. After the substitution of the elastic stresses in the Euler–Lagrange equations they become coupled and with the 1D-Poisson equation $\varepsilon_0\varepsilon_b\left(\partial^2\varphi/\partial\tilde{x}^2\right) = \partial\tilde{P}_1/\partial\tilde{x} - e\rho$. The boundary conditions to the Poisson and Euler–Lagrange and equations are $\varphi(\tilde{x} \to \pm\infty) \to 0$, $\tilde{P}_3(\tilde{x} = 0) = 0$, $\tilde{P}_3(\tilde{x} \to +\infty) = +\tilde{P}_S$ and $\tilde{P}_{1,2}(\tilde{x} \to \pm\infty) \to 0$.

6.2. Charged Domain Walls in Uniaxial Ferroelectrics

Charged head-to-head or tail-to-tail domain walls, depending on the bound charge discontinuity at the wall, ± 2 $P_S \sin\theta$, unambiguously determined by the incline angle θ between the wall plane and polarization vector of the uniaxial ferroelectric (see **Figure 13**a,b), create strong electric fields, which in turn cause free charge accumulation across the wall and sharply increase the domain wall conductivity. Wall tilt effect on the charge accumulation dominates for charged walls in comparison with the flexoelectric coupling.

The electric field and potential created by the wall bound charges ± 2 $P_S \sin\theta$ and screening electrons (proper carriers) are the highest for the perpendicular wall (incline angle $\theta = \pi/2$) with maximum bound charge 2 P_S; it decreases with decreasing θ and bound charge and vanishes at $\theta = 0$. As a result of electron accumulation, the static conductivity dramatically increases at the wall: up 3 orders of magnitude for perpendicular domain wall at $\theta = \pi/2$ to 1 order for weakly charged wall at $\theta = \pi/40$ [see Figure 13(c)]. Due to the low mobility of holes, the conductivity across the tail-to-tail wall is at least an order of magnitude smaller than the one of the head-to-head wall.[23]

There are space charge regions around the charged domain walls, but the quantitative characteristics of the regions can be very different for the tail-to-tail and head-to-head walls. In particular, for the donor doped ferroelectric semiconductor $LiNbO_3$:MgO the head-to-head wall is surrounded by the thick space charge layer with accumulated electrons and depleted donors of the thickness about 100 r_c, where r_c is the temperature-dependent correlation lengths, as shown in Figure 13d. The tail-to-tail wall is surrounded by the thin space charge layer with accumulated holes of thickness about 10 r_c and thick layer with accumulated donors of thickness about 100 r_c, as well as the layer depleted by electrons of thickness about 100 r_c.[23]

6.3. Nominally Uncharged Domain Walls in Multiaxial Ferroelectrics

The influence of the flexoelectric effect and electrostriction coupling on the nominally uncharged 180° domain wall static conductivity in tetragonal ferroelectric-semiconductor $Pb(Zr,Ti)O_3$[24] and rhombohedral $BiFeO_3$[25] and $BaTiO_3$[163] was analyzed within LGD theory. It has been shown that flexoelectric coupling induces a Neel component of polarization, $P_\perp$, that is perpendicular to the wall plane, and thus creates depolarization field that in turn leads to free carriers accumulation by the wall increasing its static conductivity. Polarization component parallel to the wall plane, $P_{\uparrow\uparrow}$, is rather weakly affected by the presence of the flexoelectric coupling. Without flexoelectric coupling only electrostriction couples polarization and elastic strains. Flexoelectric coupling impact is essential at small tilt angles corresponding to the weakly charged and nominally uncharged domain wall. Wall tilt effect on the charge accumulation dominates for charged walls.

In tetragonal ferroelectric phase the flexoelectric coupling, via the "flexoelectric" field $F_{12}\partial(\tilde{\sigma}_2 + \tilde{\sigma}_3)/\partial\tilde{x}$, leads to the appearance of polarization component perpendicular to the wall plane, $P_\perp$ and its strong gradient across the "nominally uncharged" and weakly charged domain walls. The strength of carrier accumulation/depletion at the wall plane is determined by the behaviour of electric potential. Dependences of the electric potential ϕ in a cylindrical domain in a tetragonal $PbTi_{0.8}Zr_{0.2}O_3$ and relative electron density on the domain radius R, drawn in **Figure 14**a, are shown in Figure 14b,c for positive, zero and negative flexoelectric coupling coefficient F_{12}. The flexoelectric coupling determines the type of accumulated carriers and the degree of accumulation. At $F_{12} = 0$ accumulation is absent. It is seen from the figure that cylindrical nanodomains can be conductive across the entire cross-section.

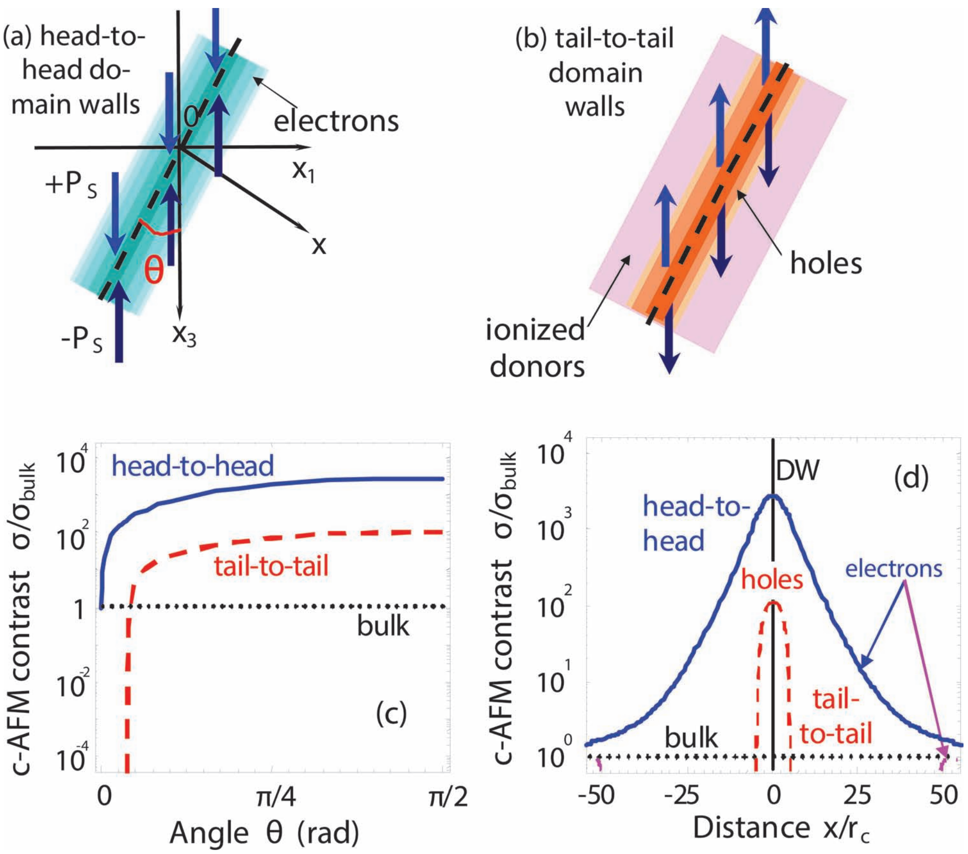

Figure 13. Sketch of the charged walls in the uniaxial ferroelectrics-semiconductors of *n*-type: a) tilted head-to-head and b) inclined tail-to-tail. The tilt angle of the domain wall is θ. c) Dependence of the relative static conductivity (c-AFM contrast) at the domain wall plane $x = 0$ calculated for tilted head-to-head (solid curve) and "tail-to-tail"(dashed curve) domain wall. d) C-AFM contrast, calculated for tilted head-to-head (solid curve) and "tail-to-tail"(dashed curve) domain wall with tilt angles $\theta = \pi/2$, bulk (dotted line). Material parameters correspond to $LiNbO_3$ with donor concentration 10^{25} m^{-3}. Flexoelectric coupling is neglected. Adapted with permission.[23]

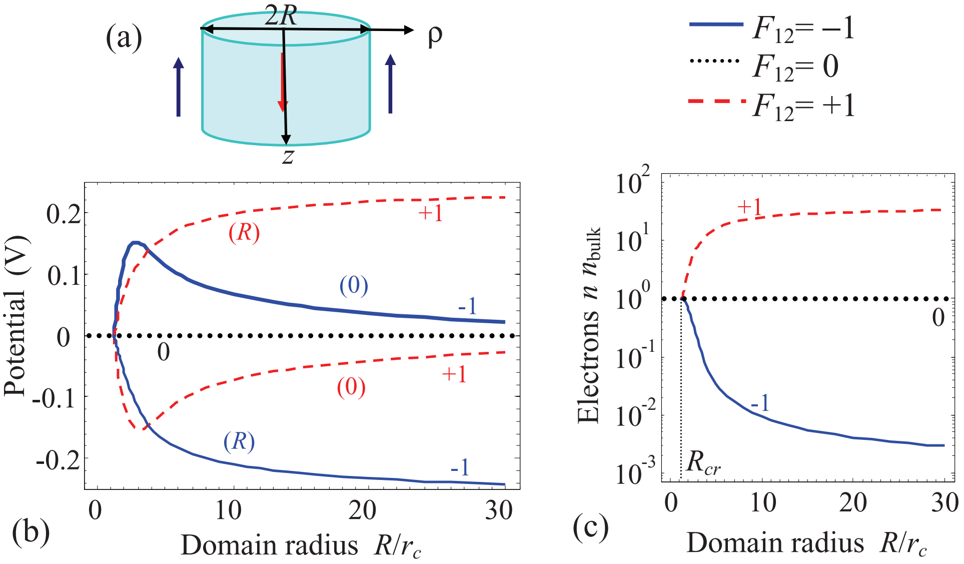

Figure 14. Impact of flexoelectric coupling on conductivity of nominally uncharged domain wall. a) Sketch of cylindrical domain. Dependence of the b) potential and c) relative electron density on the radius R of the cylindrical domain calculated for flexoelectric coupling coefficients $F_{12} = -1 \times 10^{-10}$m^3/C, 0 and $+1 \times 10^{-10}$m^3/C (numbers "–1", "+1" and "0" near the curves). Potential b) was calculated at the cylindrical domain wall ($\phi(R)$, solid curves) and in the middle of the domain ($\phi(0)$, dotted curves). Electron density was averaged across the domain wall thickness. Material parameters correspond to $PbZr_{0.2}Ti_{0.8}O_3$. Adapted with permission.[24]

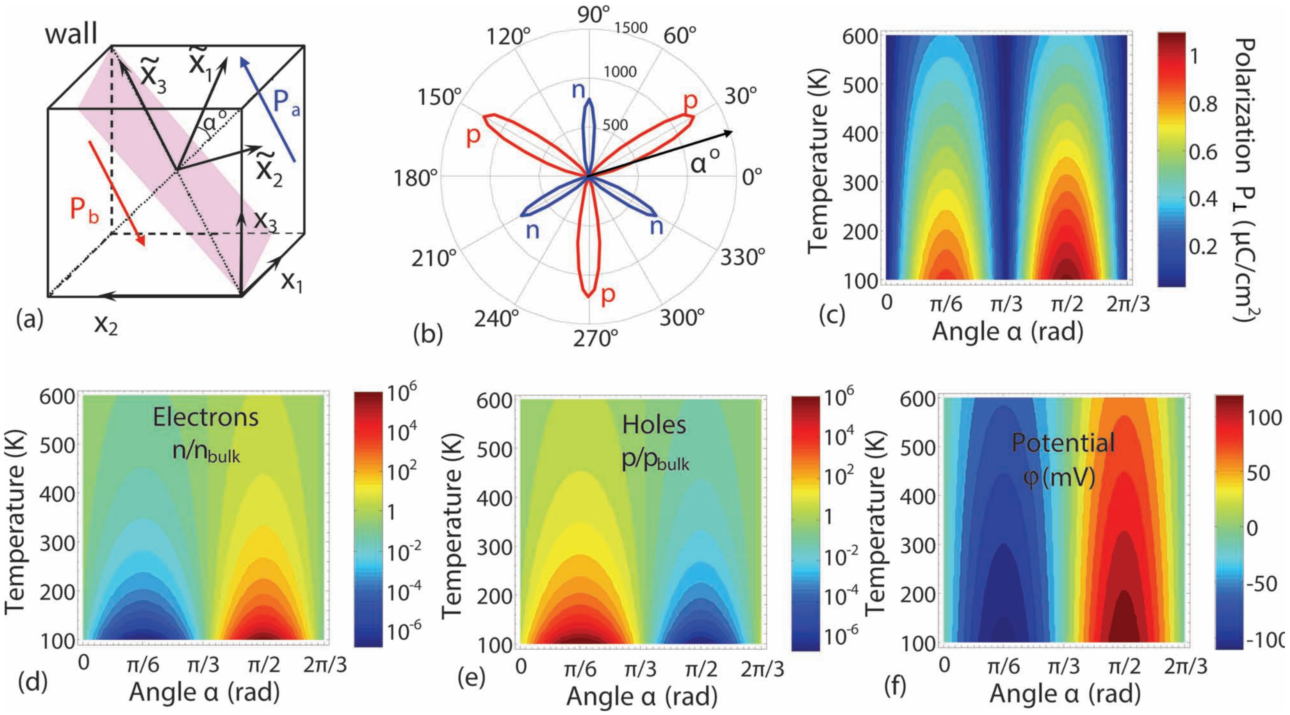

Figure 15. Anisotropic carrier accumulation at curved domain walls. a) Nominally uncharged 180° domain wall scheme in a rhombohedral ferroelectric. Wall rotation angle is α. b)Anisotropic angular dependence of carrier density at the domain wall in $BiFeO_3$ at 200 K; *n*–electrons, *p*–holes, α–wall rotation angle. c–f) Contour map in coordinates temperature - wall rotation angle of c) maximal Neel component of polarization, d) relative electron density, e) hole density and f) potential barrier/well at the nominally uncharged 180° domain walls in multiferroic. $BiFeO_3$ parameters are listed elsewhere.[25]

Implications of such conductive channels may be promising for nanoelectronics.[87]

The anisotropic nature of the carrier accumulation by nominally uncharged 180° domain walls in rhombohedral *3m*-ferroelectrics such as $BiFeO_3$ and $BaTiO_3$ follows from the strong dependence of the flexoelectric and electrostriction coefficients on the wall rotation angle α (see **Figure 15**a and refs.[25,163]) For 3m symmetry the holes density is minimal at the angles $\alpha = 3\pi/6, 7\pi/6, 11\pi/6$ and maximal at the angles $\alpha = \pi/6, 5\pi/6, 9\pi/6$, as plotted in Figure 15b–e. Bulk level corresponds to the angles $\alpha = 0, \pi/3, 2\pi/3$ (at $F_{ij} = 0$) and weakly shifts with F_{ij} increase. The situation for electrons is visa-versa. Modulation depth of the carriers accumulation/depletion is about 1–3 orders of magnitude in multiferroic $BiFeO_3$.[25] Potential barrier variation ≈50–100 mV at the wall, shown in Figure 15f, are in good agreement with the first-principles studies in $BiFeO_3$,[158] which showed that band gap narrows on the value 50 meV at uncharged 180° domain walls. To summarize LGD calculations are in qualitative agreement with experimental results[19,40,41,86,87,96] and provide a counterpart that is consistent with recent first principles calculations.

6.4. Landau Description of the Order Parameters in Hexagonal Manganites

Seminal theoretical work by Janovec and Privratska, showed the possibility of net magnetization occurring at domain walls in antiferromagnetic materials.[181–183] More recently, Landau theory of the structural, polar and magnetic ordering in hexagonal manganites was evolved by Mostovoy et al.[184] In particular in hexagonal manganites $YMnO_3$ and $ErMnO_3$ ferroelectric polarization and magnetization are coupled to the structural order parameter. Possibly the coupling leads to the flip of the polarization at the twin domains, as well as to the clamping between ferroelectric and antiferromagnetic domain walls.

Extracting Landau expansion parameters from the first-principles calculations Mostovoy et al.[184] showed that ferroelectric polarization occurs from a non-linear coupling to the trimerisation mode. In the trimerised state of $YMnO_3$ (and by continuation $ErMnO_3$) three neighbouring MnO_5 bipyramids tilt with respect to their common equatorial oxygen atom. As a consequence of the hexagonal structure of Mn-O layers, there are six distinct trimerised states, corresponding to six degenerate minima of the lattice energy. The trimerisation, that is in fact a periodic lattice modulation in a layered system, was described in continuous approach using the amplitude Q and phase Φ. The phase Φ is the angle describing the in-plane displacements of apical oxygens. The spontaneous electric polarization was regarded proportional to the amplitude of the zone-centre mode P. The free-energy expansion in powers of Q, P, Φ and their gradients, was obtained by conventional way, using the transformation properties of the trimerisation phase and the parent high-temperature space group for polarization. To describe the coupling between the ferromagnetic, structural (Q, Φ) and ferroelectric (P) order parameters at the domain walls, the symmetry of the magnetic order parameter should be established.

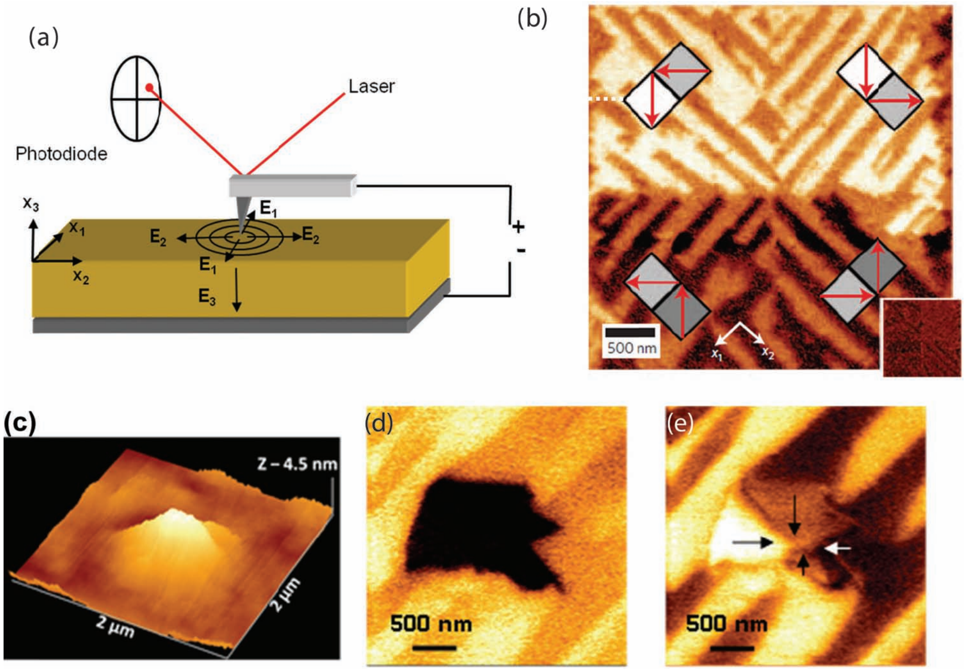

Figure 16. Formation of topological defects. a) Schematic display of radially symmetric electric field around a biased SPM tip. This symmetry can be broken by motion of the tip, or by existing domain walls. b) A star domain pattern formed by deterministic ferroelastic switching by selective tip motion. The application of a bias pulse through the tip can also lead to topological defects such as the center-type domains shown in the c) topography, d) vertical PFM, and e) lateral PFM images. b) Reproduced with permission.[197] Copyright 2009, from Macmillan Publishers Ltd. c–e) Reproduced with permission.[198] Copyright 2011, American Chemical Society.

Mostovoy et al.[184] showed that the structure of magnetization across the domain walls can be described by two angles ψ_1 and ψ_2, corresponding to the spins rotation around the c axis in the even and odd layers of $YMnO_3$ respectively.

7. Conductance of 1D Topological Defects

Most studies to date have explored the properties of 2D topological defects such as ferroic domain walls. At the same time, implementation in electronic devices requires the capability to create and modify 1D conductive objects, effectively creating "wiring" in functional devices. The existence of 1D topological defects, namely vortices, have been reported in ferroelectric systems and has led to a number of experimental[185–188] and theoretical efforts[189–193] aimed at visualization of these defects and probing their properties. Most recent studies confirm the existence of vortices or flux-closure domains in ferroelectrics through direct imaging using transmission electron microscopy.[188,194–196] In all these reports, the vortices have been observed in ferroelectric nanostructures, in as-grown thin films or single crystals. However, it is of great interest to make vortices systematically, and furthermore to characterize the properties of such topological defects.

7.1. Domain Manipulation: Forming Vortices and Defects

The electric field around a biased SPM tip is highly non-uniform and consists of out-of-plane (OP) and in-plane (IP) field components relative to the sample surface (**Figure 16**a), thus affecting both in-plane and out of plane components of polarization. In this regard, it is interesting to analyze feasibility for in-plane polarization control. From the theoretical viewpoint, polarization switching in rhombohedral materials is a problem of selection between thermodynamically equivalent pathways, with switching proceeding via either 180°, 109° or 71° rotation of the polarization vector. The field created by the tip has in-plane components that are radially symmetric, so polarization switching induced by a biased, stationary tip (in the absence of defects) does not allow for deterministic selection of the in-plane polarization direction. Moving the tip whilst applying a bias, however, can break this symmetry and lead to control of in-plane (IP) switching, as demonstrated by Balke et al.[197] Depending on the direction of tip motion during biasing, exotic domain patterns, such as the 'star' pattern shown in Figure 16b, can be formed. Topological defects can also be formed by exploiting the symmetry-breaking ability of existing domain walls in the material.[198] In some cases, simply applying a large bias to the tip can be enough to induce formation of topological defects, such as the center-type domain pattern seen in Figure 16c–e,[198] where the polarization components couple with the in-plane directions of the applied field.[199] Regardless of how they are formed, however, the crucial aspect of the topological defect is the unique properties arising at such sites.

Here, we explore the unique electric conduction found in ferroelectric vortices and antivortices, formed by the biased tip motion along specific directions as described above.[86] Note

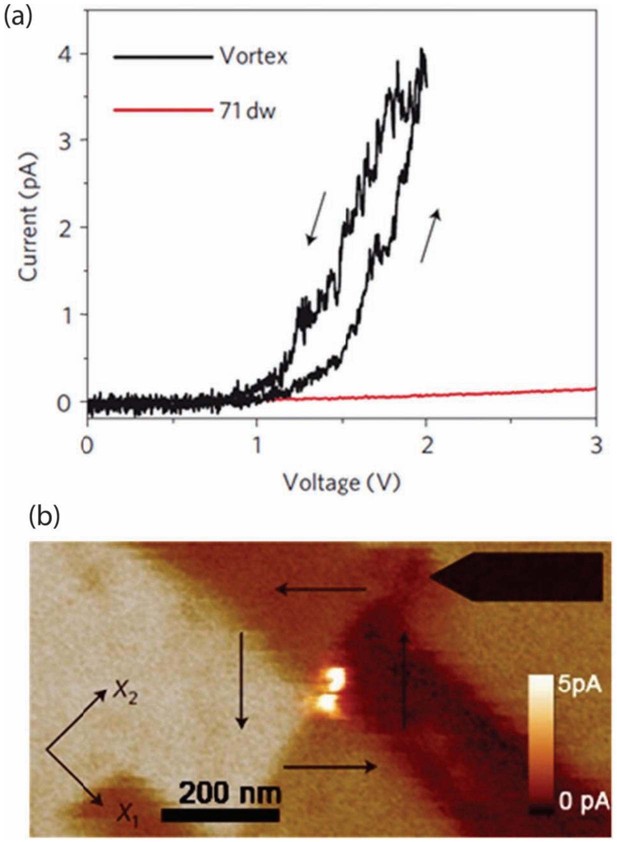

Figure 17. Conduction at vortex core. a) *I–V* curves collected on as-grown 71° domain walls and at the vortex core. b) In-plane PFM image showing a ferroelectric vortex overlaid with a conductive AFM image showing enhanced conductivity at the vortex core. Polarization directions are marked with arrows. Reproduced with permission.[86] Copyright 2011, Macmillan Publishers Ltd.

that the 'vortex' in this context denotes the center of a closure domain formed by the in-plane polarization components of four ferroelectric domains which are aligned head-to-tail, and can formally be described by a planar spin configuration with a winding number of +1.[3] The anti-vortex is defined as a domain arrangement where the in-plane polarization components point towards and away from each other forming a nominally charged point at the four-domain junction (winding number -1).[3]

We would like to point out that the classification of some of the exotic domain patterns and topological defects in this field is variable. Some groups[200] exclusively use the term vortex for those patterns that exhibit nonzero curl; in this sense a closure domain pattern with winding number +1 is not strictly a vortex, although other groups[132,201] (including the authors)[86,197] have used this terminology. The reason is to emphasize the topological nature of these defects. On the other hand, others[16,188] use the term 'vertex' to describe these domain junctions. Regardless, experimentally these are very difficult to distinguish (with SPM techniques), and the term vortex is used widely to describe domain patterns with winding number +1 irrespective of curl.[202–204]

7.2. Transport Through a Ferroelectric Vortex

To characterize the local electronic properties of the ferroelectric vortex, we employed conductive AFM imaging and single-point *I–V* measurements. **Figure 17**a shows the *I–V* curves collected at the as-grown 71° domain wall and at the vortex core. The four domain junction exhibits a higher conductivity, with significant conduction observed above ≈1 V biases as compared to >3 V at the as-grown domain wall. The shown *I–V* curve is reproducible if the voltages are kept low (<2 V) and has been measured at several vortex and anti-vortex cores. There does not seem to be a different conduction behavior for vortex or anti-vortex domain configurations. Figure 17b displays the conductive AFM image recorded at 2 V_{dc} bias overlaid on the IP-PFM image. Here, it can be clearly seen that the area around the vortex core shows enhanced conductivity, thus demonstrating the potential to use ferroelectric vortices as 1D conduction channels. The IP PFM image after the current measurements confirms that the domain pattern was not irreversibly changed during bias application. However, the application of voltages > 2 V often leads to the irreversible reconstruction of domain structure and therefore the topological defects.

7.3. Theory of Vortex Conduction

The localized conductivity at the vortex and anti-vortex cores can arise from multiple factors, including static changes of electronic structure due to higher symmetry at topological defects, static effects related to charge and strain at the vortex core, and dynamics effects related to field-dynamics of the vortex. Effective Hamiltonian Monte Carlo simulations[205] of vortex in BFO nanodots predict that the magnitude of electric dipoles and oxygen octahedral tiltings becomes smaller by 7% and 2% respectively, compared to the bulk. Using these structural changes as an input for density functional theory (DFT), the vortex is predicted to have downward shift of the conduction band edge by around 0.173 eV (in comparison to the zero band gap for metallic phase).[206] This indicates that purely electronic effects are insufficient to account for observed conductance enhancement.

The static and dynamic structure of the topological defects was further explored by phase field modeling. The static domain structure and associated electric field, potential, and strain are shown in **Figure 18**. Note that the vortex core is associated with significant tensile strain, as expected for a disclination center, and has high electrostatic potential. Note that strain values can also be approximated assuming zero polarization at the vortex core, $u_{ij}(\mathbf{r}) \sim Q_{ijkl}\left(P_k(\mathbf{r})\,P_l(\mathbf{r}) - P_k^S P_l^S\right)$, where $u^{\max}{}_{22} = Q_{12}\,P^2{}_S \approx -0.016$ and $Q_{11} \approx 0.032$ $\mathrm{m^4/C^2}$,$Q_{11} \approx -0.016$ $\mathrm{m^4/C^2}$ is electrostriction tensor, $P_k(\mathbf{r})$ is polarization vector, $P^S{}_k$ ≈1 $\mathrm{C/m^2}$ is spontaneous polarization far from the BFO wall. These values allow to estimate electron/hole and vacancy segregation at the vortex core, as analyzed in depth in Ref.[86] Specifically, for vortex excess free energy for vacancy segregation is 160 mV, as compared to 40 mV for domain wall, and excess potential is 360 mV vs 170 mV for the wall. Vortex core (on average) shows strong propensity to vacancy segregation driven by elastic fields. At the same time, antivortices are prone to the

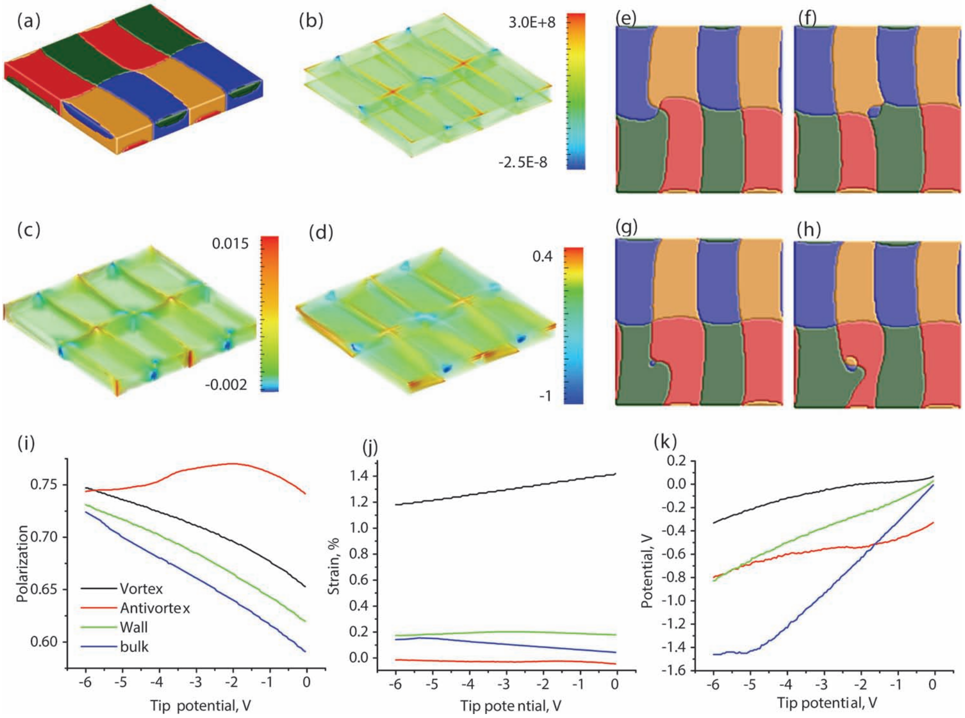

Figure 18. Phase-field simulations of vortex and anti-vortex states a) Domain structure, b) electric field, c) trace of the strain tensor, and d) potential for vortex-antivortex lattice. Typical domain configuration for tip-induced switching at the e) vortex, f) antivortex, g) domain wall, and h) domain for a bias of –6.0 V (top view). Evolution of electroelastic fields at the defects as a function of tip potential for (i) average polarization, (j) strain, and (k) potential. Note that tip potential in simulations is negative, corresponding to positive biases applied experimentally to bottom electrodes. Reproduced with permission.[86] Copyright 2011, Macmillan Publishers Ltd.

hole segregation. However, the absolute signs of the effects are countervailing.

Finally, phase field allows for dynamic effect to be explored. For vortex and wall the dominant mode of evolution is the twist of the in-plane polarization component, in agreement with previous studies.[108,187,197,207] The dynamics can be parameterized by voltage dependence of average (through thickness) polarization and average potential. The low potentials at the vortex and antivortex cores are the result of effective screening by polarization redistribution and formation of the charged domains walls. These charged walls span the thickness of the sample and provide the conduction channels[23] and are relatively insensitive to the details of carrier segregation mechanism. The vortex core is therefore a dynamic conductor and it raises a possibility of a 1D conduction channel through the whole thickness of the $BiFeO_3$ film.

8. Summary

Structure, properties, and dynamics of topological defects in order parameter fields offer a fascinating window in the physics of condensed matter systems, with examples ranging from liquid crystals to superconductors to surface and bulk phases to ferroics. In many cases, it is the defects that define macroscopic functionality either through macroscopically averaged responses over multiple non-interacting defects, or emergent phenomena due to defect-defect interactions. However, while observations of domain structures and hence topological defects were feasible for multiple decades,[10,145] its internal structure and local properties has long remained elusive.

Recent advances in high-resolution electron microscopy have allowed visualizing the internal structure of topological defects in ferroelectric and ferroelastic materials.[148,195,208,209] At the same time, emergence of scanning probe microscopy techniques with multiple modalities of local detection has opened the pathway for systematic study and in many cases controlled design and creation of topological defects. The conductive domain walls and vortex cores in ferroelectric materials offer a beautiful example of the systems in which ferroelectric and transport properties can be explored in real space locally, and further correlated with structural studies. The future will undoubtedly see the combined in situ studies of domain wall structure and functionality enabled by rapidly emergent combined SPM-STEM methods.[210–213]

Acknowledgements

R.K.V. and V.N. acknowledge support of ARC Discovery Project Scheme, ARC LIEF and the user facilities at ORNL-CNMS under user proposal No. 2011-283. W.W. acknowledges support from NSF DMR Award no. DMR-0844807.Use of the Center for Nanoscale Materials was supported by the U. S. Department of Energy, Office of Science, Office of Basic Energy Sciences, under Contract No. DE-AC02-06CH11357.SVK, N.B., P.M. and A.P.B. acknowledge support from the Scientific User Facilities Division, DOE BES. P.M. acknowledges Wigner fellowship of ORNL.

Received: January 9, 2013
Published online: April 11, 2013

---

[1] M. Cruz, N. Turok, P. Vielva, E. Martinez-Gonzalez, M. Hobson, *Science* **2007**, *318*, 1612.
[2] C. Sátiro, F. Moraes, *Eur. Phys. J. E: Soft Matter Biol. Phys.* **2006**, *20*, 173.
[3] N. D. Mermin, *Rev. Mod. Phys.* **1979**, *51*, 591.
[4] S. M. Griffin, M. Lilienblum, K. T. Delaney, Y. Kumagai, M. Fiebig, N. A. Spaldin, *Physical Review X* **2012**, *2*, 041022.
[5] G. Blatter, M. V. Feigel'man, V. B. Geshkenbein, A. I. Larkin, V. M. Vinokur, *Rev. Mod. Phys.* **1994**, *66*, 1125.
[6] Y. Ran, Y. Zhang, A. Vishwanath, *Nat. Phys.* **2009**, *5*, 298.
[7] A. G. Khachaturyan, J. W. Morris Jr., *Phys. Rev. Lett.* **1987**, *59*, 2776.
[8] J. F. Scott, M. Dawber, *Appl. Phys. Lett.* **2000**, *76*, 3801.
[9] T. C. L. P. M. Chaikin, *Principles of Condensed Matter Physics*, Cambridge, Cambridge **1995**.
[10] A. K. Tagantsev, L. E. Cross, J. Fousek, *Domains in Ferroic Crystals and Thin Films*, Springer, New York **2010**.
[11] E. Salje, H. Zhang, *Phase Transitions* **2009**, *82*, 452.
[12] Q. He, C. H. Yeh, J. C. Yang, G. Singh-Bhalla, C. W. Liang, P. W. Chiu, G. Catalan, L. W. Martin, Y. H. Chu, J. F. Scott, R. Ramesh, *Phys. Rev. Lett.* **2012**, *108*, 067203.
[13] Q. He, Y. H. Chu, J. T. Heron, S. Y. Yang, W. I. Liang, C. Y. Kuo, H. J. Lin, P. Yu, C. W. Liang, R. J. Zeches, W. C. Kuo, J. Y. Juang, C. T. Chen, E. Arenholz, A. Scholl, R. Ramesh, *Nat. Commun.* **2011**, *2*, 225.
[14] S. Y. Yang, J. Seidel, S. J. Byrnes, P. Shafer, C. H. Yang, M. D. Rossell, P. Yu, Y. H. Chu, J. F. Scott, J. W. Ager, L. W. Martin, R. Ramesh, *Nat. Nanotechnol.* **2010**, *5*, 143.
[15] A. Chanthbouala, V. Garcia, R. O. Cherifi, K. Bouzehouane, S. Fusil, X. Moya, S. Xavier, H. Yamada, C. Deranlot, N. D. Mathur, M. Bibes, A. Barthélémy, J. Grollier, *Nat. Mater.* **2012**, *11*, 860.
[16] G. Catalan, J. Seidel, R. Ramesh, J. F. Scott, *Rev. Mod. Phys.* **2012**, *84*, 119.
[17] J. Lajzerowicz, J. Niez, *J. Physique Lett.* **1979**, *40*, 165.
[18] B. M. Vul, G. M. Guro, I.I. Ivanchik, *Ferroelectrics* **1973**, *6*, 29.
[19] J. Seidel, L. W. Martin, Q. He, Q. Zhan, Y. H. Chu, A. Rother, M. E. Hawkridge, P. Maksymovych, P. Yu, M. Gajek, N. Balke, S. V. Kalinin, S. Gemming, F. Wang, G. Catalan, J. F. Scott, N. A. Spaldin, J. Orenstein, R. Ramesh, *Nat. Mater.* **2009**, *8*, 229.
[20] P. Maksymovych, J. Seidel, Y. H. Chu, P. Wu, A. P. Baddorf, L.-Q. Chen, S. V. Kalinin, R. Ramesh, *Nano Lett.* **2011**, *11*, 1906.
[21] M. Y. Gureev, A. K. Tagantsev, N. Setter, *Phys. Rev. B* **2011**, *83* 184104.
[22] T. Sluka, A. K. Tagantsev, D. Damjanovic, M. Gureev, N. Setter, *Nat. Commun.* **2012**, *3*, 748.
[23] E. A. Eliseev, A. N. Morozovska, G. S. Svechnikov, V. Gopalan, V. Y. Shur, *Phys. Rev. B* **2011**, *83*, 235313.
[24] E. A. Eliseev, A. N. Morozovska, G. S. Svechnikov, P. Maksymovych, S. V. Kalinin, *Phys. Rev. B* **2012**, *85*, 045312.
[25] A. N. Morozovska, R. K. Vasudevan, P. Maksymovych, S. V. Kalinin, E. A. Eliseev, *Phys. Rev. B* **2012**, *86*, 085315.
[26] A. K. Tagantsev, E. B. Sonin, *Ferroelectrics* **1989**, *98*, 297.
[27] E. B. Sonin, A. K. Tagantsev, *Ferroelectrics* **1989**, *98*, 291.
[28] E. B. Sonin, A. K. Tagantsev, *Zh. Eksp. Teor. Fiz.* **1988**, *94*, 315.
[29] M. Daraktchiev, G. Catalan, J. F. Scott, *Phys. Rev. B* **2010**, *81*.
[30] J. Salafranca, R. Yu, E. Dagotto, *Phys. Rev. B* **2010**, *81*, 245122.
[31] L. Goncalves-Ferreira, S. A. T. Redfern, E. Artacho, E. Salje, W. T. Lee, *Phys. Rev. B* **2010**, *81*.
[32] Y. Kim, M. Alexe, E. K. H. Salje, *Appl. Phys. Lett.* **2010**, *96*, 032904.
[33] A. Lubk, S. Gemming, N. A. Spaldin, *Phys. Rev. B* **2009**, *80*, 104110.
[34] A. Tselev, V. Meunier, E. Strelcov, W. A. Shelton, I. A. Luk'yanchuk, K. Jones, R. Proksch, A. Kolmakov, S. V. Kalinin, *ACS Nano* **2010**, *4*, 4412.
[35] I. Vrejoiu, G. Le Rhun, L. Pintilie, D. Hesse, M. Alexe, U. Gösele, *Adv. Mater.* **2006**, *18*, 1657.
[36] M. Abplanalp, L. M. Eng, P. Günter, *Appl. Phys. A: Mater. Sci. Process.* **1998**, *66*, S231.
[37] A. Roelofs, U. Bottger, R. Waser, F. Schlaphof, S. Trogisch, L. M. Eng, *Appl. Phys. Lett.* **2000**, *77*, 3444.
[38] T. Jungk, Á. Hoffmann, E. Soergel, *Appl. Phys. Lett.* **2006**, *89*, 042901.
[39] A. Gruverman, A. Kholkin, A. Kingon, H. Tokumoto, *Appl. Phys. Lett.* **2001**, *78*, 2751.
[40] S. Farokhipoor, B. Noheda, *Phys. Rev. Lett.* **2011**, *107* 127601.
[41] J. Guyonnet, I. Gaponenko, S. Gariglio, P. Paruch, *Adv. Mater.* **2011**, *23*, 5377.
[42] S. V. Kalinin, B. J. Rodriguez, A. Y. Borisevich, A. P. Baddorf, N. Balke, J. Chang Hye, L.-Q. Chen, S. Choudhury, S. Jesse, P. Maksymovych, M. P. Nikiforov, S. J. Pennycook, *Adv. Mater.* **2010**, *22*, 314.
[43] S. V. Kalinin, S. Jesse, B. J. Rodriguez, Y. H. Chu, R. Ramesh, E. A. Eliseev, A. N. Morozovska, *Phys. Rev. Lett.* **2008**, *100*, 155703.
[44] A. Gruverman, A. Kholkin, *Rep. Prog. Phys.* **2006**, *69*, 2443.
[45] S. Jesse, B. J. Rodriguez, S. Choudhury, A. P. Baddorf, I. Vrejoiu, D. Hesse, M. Alexe, E. A. Eliseev, A. N. Morozovska, J. Zhang, L.-Q. Chen, S. V. Kalinin, *Nat. Mater.* **2008**, *7*, 209.
[46] I. Tanaka, I. Kamiya, H. Sakaki, N. Qureshi, S. Allen, P. Petroff, *Appl. Phys. Lett.* **1999**, *74*, 844.
[47] A. Olbrich, B. Ebersberger, C. Boit, J. Vancea, H. Hoffmarm, *Microelectronics Reliability* **1999**, *39*, 941.
[48] H. Kado, T. Tohda, *Appl. Phys. Lett.* **1995**, *66*, 2961.
[49] A. Gruverman, O. Kolosov, J. Hatano, K. Takahashi, H. Tokumoto, *J. Vac. Sci. Technol., B* **1995**, *13*, 1095.
[50] O. Kolosov, A. Gruverman, J. Hatano, K. Takahashi, H. Tokumoto, *Phys. Rev. Lett.* **1995**, *74*, 4309.
[51] A. Gruverman, O. Auciello, H. Tokumoto, *Integr. Ferroelectr.* **1998**, *19*, 49.
[52] E. L. Colla, S. Hong, D. V. Taylor, A. K. Tagantsev, N. Setter, K. No, *Appl. Phys. Lett.* **1998**, *72*, 2763.
[53] C. S. Ganpule, V. Nagarajan, H. Li, A. S. Ogale, D. E. Steinhauer, S. Aggarwal, E. Williams, R. Ramesh, P. De Wolf, *Appl. Phys. Lett.* **2000**, *77*, 292.
[54] C. S. Ganpule, V. Nagarajan, B. K. Hill, A. L. Roytburd, E. D. Williams, R. Ramesh, S. P. Alpay, A. Roelofs, R. Waser, L. M. Eng, *J. Appl. Phys.* **2002**, *91*, 1477.
[55] V. Nagarajan, A. Roytburd, A. Stanishevsky, S. Prasertchoung, T. Zhao, L. Chen, J. Melngailis, O. Auciello, R. Ramesh, *Nat. Mater.* **2003**, *2*, 43.
[56] F. Zavaliche, R. R. Das, D. M. Kim, C. B. Eom, S. Y. Yang, P. Shafer, R. Ramesh, *Appl. Phys. Lett.* **2005**, *87*, 182912.
[57] C. Harnagea, A. Pignolet, M. Alexe, D. Hesse, *Integr. Ferroelectr.* **2002**, *44*, 113.
[58] L. Eng, S. Grafström, C. Loppacher, F. Schlaphof, S. Trogisch, A. Roelofs, R. Waser, *Adv. Solid State Phys.* **2001**, 287.
[59] M. Basletic, J. L. Maurice, C. Carrétéro, G. Herranz, O. Copie, M. Bibes, É. Jacquet, K. Bouzehouane, S. Fusil, A. Barthélémy, *Nat. Mater.* **2008**, *7*, 621.
[60] Y. H. Hsieh, J. M. Liou, B. C. Huang, C. W. Liang, Q. He, Q. Zhan, Y. P. Chiu, Y. C. Chen, Y. H. Chu, *Adv. Mater.* **2012**, *24*, 4564.
[61] R. K. Vasudevan, S. Jesse, Y. Kim, A. Kumar, S. V. Kalinin, *MRS Commun.* **2012**, *2*, 61.
[62] Y. W. So, D. J. Kim, T. W. Noh, J.-G. Yoon, T. K. Song, *Appl. Phys. Lett.* **2005**, *86*, 092905.

[63] V. V. Shvartsman, A. L. Kholkin, A. Orlova, D. Kiselev, A. A. Bogomolov, A. Sternberg, *Appl. Phys. Lett.* **2005**, *86*, 202907.
[64] V. V. Shvartsman, N. A. Pertsev, J. M. Herrero, C. Zaldo, A. L. Kholkin, *J. Appl. Phys.* **2005**, *97*, 104105.
[65] A. Gruverman, B. J. Rodriguez, C. Dehoff, J. D. Waldrep, A. I. Kingon, R. J. Nemanich, J. S. Cross, *Appl. Phys. Lett.* **2005**, *87*, 082902.
[66] A. Agronin, M. Molotskii, Y. Rosenwaks, G. Rosenman, B. J. Rodriguez, A. I. Kingon, A. Gruverman, *J. Appl. Phys.* **2006**, *99*, 104102.
[67] M. Gajek, M. Bibes, S. Fusil, K. Bouzehouane, J. Fontcuberta, A. Barthelemy, A. Fert, *Nat. Mater.* **2007**, *6*, 296.
[68] S. Valencia, A. Crassous, L. Bocher, V. Garcia, X. Moya, R. O. Cherifi, C. Deranlot, K. Bouzehouane, S. Fusil, A. Zobelli, A. Gloter, N. D. Mathur, A. Gaupp, R. Abrudan, F. Radu, A. Barthélémy, M. Bibes, *Nat. Mater.* **2011**, *10*, 753.
[69] D. B. Strukov, G. S. Snider, D. R. Stewart, R. S. Williams, *Nature* **2008**, *453*, 80.
[70] S. John Paul, B. S. Dmitri, B. Julien, J. J. Yang, M.-R. Gilberto, R. S. Williams, *Nanotechnology* **2011**, *22*, 254015.
[71] J. J. Yang, M. D. Pickett, X. Li, D. A. A. Ohlberg, D. R. Stewart, R. S. Williams, *Nat. Nano.* **2008**, *3*, 429.
[72] D. J. Kim, H. Lu, S. Ryu, C. W. Bark, C. B. Eom, E. Y. Tsymbal, A. Gruverman, *Nano Lett.* **2012**.
[73] Y. Kim, A. N. Morozovska, A. Kumar, S. Jesse, E. A. Eliseev, F. Alibart, D. Strukov, S. V. Kalinin, *ACS Nano* **2012**, *6*, 7026.
[74] N. Balke, A. Tselev, T. M. Arruda, S. Jesse, Y.-H. Chu, S. V. Kalinin, *ACS Nano* **2012**, *6*, 10139.
[75] S. V. Kalinin, S. Jesse, A. Tselev, A. P. Baddorf, N. Balke, *ACS Nano* **2011**, *5*, 5683.
[76] A. Kumar, T. M. Arruda, Y. Kim, I. N. Ivanov, S. Jesse, C. W. Bark, N. C. Bristowe, E. Artacho, P. B. Littlewood, C.-B. Eom, S. V. Kalinin, *ACS Nano* **2012**, *6*, 3841.
[77] H. D. Chen, K. R. Udayakumar, K. K. Li, C. J. Gaskey, L. E. Cross, *Integr. Ferroelectr.* **1997**, *15*, 89.
[78] I. Stolichnov, A. Tagantsev, N. Setter, S. Okhonin, P. Fazan, J. S. Cross, M. Tsukada, *J. Appl. Phys.* **2000**, *87*, 1925.
[79] J. Suntivich, K. J. May, H. A. Gasteiger, J. B. Goodenough, Y. Shao-Horn, *Science* **2011**, *334*, 1383.
[80] R. Merkle, J. Maier, *Angew. Chem. Int. Ed.* **2008**, *47*, 3874.
[81] L. Wang, R. Merkle, J. Maier, T. Acarturk, U. Starke, *Appl. Phys. Lett.* **2009**, *94*, 071908.
[82] J. Shin, V. B. Nascimento, G. Geneste, J. Rundgren, E. W. Plummer, B. Dkhil, S. V. Kalinin, A. P. Baddorf, *Nano Lett.* **2009**, *9*, 3720.
[83] P. Maksymovych, N. Balke, S. Jesse, M. Huijben, R. Ramesh, A. P. Baddorf, S. V. Kalinin, *J. Mater. Sci.* **2009**, *44*, 5095.
[84] B. Melanie, H. Volker, B. Manfred, G. Mathias, B. Ulrich, W. Roland, *J. Phys.: Condens. Matter* **2003**, *15*, 957.
[85] E. A. Eliseev, A. N. Morozovska, Y. Gu, A. Y. Borisevich, L.-Q. Chen, V. Gopalan, S. V. Kalinin, *Phys. Rev. B* **2012**, *86*, 085416.
[86] N. Balke, B. Winchester, W. Ren, Y. H. Chu, A. N. Morozovska, E. A. Eliseev, M. Huijben, R. K. Vasudevan, P. Maksymovych, J. Britson, S. Jesse, I. Kornev, R. Ramesh, L. Bellaiche, L. Q. Chen, S. V. Kalinin, *Nat. Phys.* **2012**, *8*, 81.
[87] P. Maksymovych, A. N. Morozovska, P. Yu, E. A. Eliseev, Y.-H. Chu, R. Ramesh, A. P. Baddorf, S. V. Kalinin, *Nano Lett.* **2011**, *12*, 209.
[88] J. Seidel, P. Maksymovych, Y. Batra, A. Katan, S. Y. Yang, Q. He, A. P. Baddorf, S. V. Kalinin, C. H. Yang, J. C. Yang, Y. H. Chu, E. K. H. Salje, H. Wormeester, M. Salmeron, R. Ramesh, *Phys. Rev. Lett.* **2010**, *105*.
[89] M. Schröder, A. Haußmann, A. Thiessen, E. Soergel, T. Woike, L. M. Eng, *Adv. Funct. Mater.* **2012**, *22*, 3936.
[90] W. Wu, Y. Horibe, N. Lee, S. W. Cheong, J. R. Guest, *Phys. Rev. Lett.* **2012**, *108*, 077203.
[91] D. Meier, J. Seidel, A. Cano, K. Delaney, Y. Kumagai, M. Mostovoy, N. A. Spaldin, R. Ramesh, M. Fiebig, *Nat. Mater.* **2012**, *11*, 284.
[92] S. Farokhipoor, B. Noheda, *J. Appl. Phys.* **2012**, *112*, 052003.
[93] R. J. Zeches, M. D. Rossell, J. X. Zhang, A. J. Hatt, Q. He, C. H. Yang, A. Kumar, C. H. Wang, A. Melville, C. Adamo, G. Sheng, Y. H. Chu, J. F. Ihlefeld, R. Erni, C. Ederer, V. Gopalan, L. Q. Chen, D. G. Schlom, N. A. Spaldin, L. W. Martin, R. Ramesh, *Science* **2009**, *326*, 977.
[94] S. S. P. Parkin, M. Hayashi, L. Thomas, *Science* **2008**, *320*, 190.
[95] E. K. H. Salje, *ChemPhysChem* **2010**, *11*, 940.
[96] R. K. Vasudevan, A. N. Morozovska, E. A. Eliseev, J. Britson, J. C. Yang, Y. H. Chu, P. Maksymovych, L. Q. Chen, V. Nagarajan, S. V. Kalinin, *Nano Lett.* **2012**.
[97] K. Szot, W. Speier, G. Bihlmayer, R. Waser, *Nat. Mater.* **2006**, *5*, 312.
[98] S. Menzel, M. Waters, A. Marchewka, U. Böttger, R. Dittmann, R. Waser, *Adv. Funct. Mater.* **2011**, *21*, 4487.
[99] N. B. Gharb, S. Trolier-McKinstry, D. Damjanovic, *J. Appl. Phys.* **2006**, *100*, 044107.
[100] T. J. Yang, V. Gopalan, P. J. Swart, U. Mohideen, *Phys. Rev. Lett.* **1999**, *82*, 4106.
[101] R. K. Vasudevan, M. B. Okatan, C. Duan, Y. Ehara, H. Funakubo, A. Kumar, S. Jesse, L.-Q. Chen, S. V. Kalinin, V. Nagarajan, *Adv. Func. Mater.* **2013**, *23*, 81.
[102] H. Kronmüller, *J. Phys. Colloque* **1971**, *32*, 390.
[103] O. Boser, *J. Appl. Phys.* **1987**, *62*, 1344.
[104] P. Paruch, T. Giamarchi, J. M. Triscone, *Phys. Rev. Lett.* **2005**, *94*, 197601.
[105] D. Damjanovic, *J. Appl. Phys.* **1997**, *82*, 1788.
[106] V. R. Aravind, A. N. Morozovska, S. Bhattacharyya, D. Lee, S. Jesse, I. Grinberg, Y. L. Li, S. Choudhury, P. Wu, K. Seal, A. M. Rappe, S. V. Svechnikov, E. A. Eliseev, S. R. Phillpot, L. Q. Chen, V. Gopalan, S. V. Kalinin, *Phys. Rev. B* **2010**, *82*, 024111.
[107] A. N. Morozovska, S. V. Kalinin, E. A. Eliseev, V. Gopalan, S. V. Svechnikov, *Phys. Rev. B* **2008**, *78*, 125407.
[108] V. Anbusathaiah, S. Jesse, M. Arredondo, F. Kartawidjaja, O. Ovchinnikov, J. Wang, S. V. Kalinin, V. Nagarajan, *Acta Mater.* **2010**, *58*, 5316.
[109] S. H. Jo, T. Chang, I. Ebong, B. B. Bhadviya, P. Mazumder, W. Lu, *Nano Lett.* **2010**, *10*, 1297.
[110] M. Y. Zhuravlev, R. F. Sabirianov, S. S. Jaswal, E. Y. Tsymbal, *Phys. Rev. Lett.* **2005**, *94*, 246802.
[111] F. Xu, S. Trolier-McKinstry, W. Ren, B. Xu, Z. L. Xie, K. J. Hemker, *J. Appl. Phys.* **2001**, *89*, 1336.
[112] V. Y. Shur, V. Kozhevnikov, D. Pelegov, E. Nikolaeva, E. Shishkin, *Phys. Solid State* **2001**, *43*, 1128.
[113] J. F. Ihlefeld, N. J. Podraza, Z. K. Liu, R. C. Rai, X. Xu, T. Heeg, Y. B. Chen, J. Li, R. W. Collins, J. L. Musfeldt, X. Q. Pan, J. Schubert, R. Ramesh, D. G. Schlom, *Appl. Phys. Lett.* **2008**, *92*, 142908.
[114] M. Wiegel, M. Hamoumi, G. Blasse, *Mater. Chem. Phys.* **1994**, *36*, 289.
[115] M. Nowak, B. Kauch, P. Szperlich, *Rev. Sci. Instrum.* **2009**, *80*, 046107.
[116] J. R. Contreras, H. Kohlstedt, U. Poppe, R. Waser, C. Buchal, N. A. Pertsev, *Appl. Phys. Lett.* **2003**, *83*, 4595.
[117] A. Gruverman, D. Wu, H. Lu, Y. Wang, H. Jang, C. Folkman, M. Y. Zhuravlev, D. Felker, M. Rzchowski, C. B. Eom, *Nano Lett.* **2009**, *9*, 3539.
[118] A. Chanthbouala, A. Crassous, V. Garcia, K. Bouzehouane, S. Fusil, X. Moya, J. Allibe, B. Dlubak, J. Grollier, S. Xavier, C. Deranlot, A. Moshar, R. Proksch, N. D. Mathur, M. Bibes, A. Barthelemy, *Nat. Nanotechnol.* **2012**, *7*, 101.
[119] A. Crassous, V. Garcia, K. Bouzehouane, S. Fusil, A. H. G. Vlooswijk, G. Rispens, B. Noheda, M. Bibes, A. Barthelemy, *Appl. Phys. Lett.* **2010**, *96*, 042901.

[120] M. Hambe, A. Petraru, N. A. Pertsev, P. Munroe, V. Nagarajan, H. Kohlstedt, *Adv. Funct. Mat.* **2010**, *20*, 2436.
[121] M. Gajek, M. Bibes, S. Fusil, K. Bouzehouane, J. Fontcuberta, A. Barthélémy, A. Fert, *Nat. Mater.* **2007**, *6*, 296.
[122] D. Pantel, S. Goetze, D. Hesse, M. Alexe, *Nat. Mater.* **2012**, *11*, 289.
[123] A. Q. Jiang, C. Wang, K. J. Jin, X. B. Liu, J. F. Scott, C. S. Hwang, T. A. Tang, H. B. Lu, G. Z. Yang, *Adv. Mater.* **2011**, *23*, 1277.
[124] Y. Maeno, T. Ando, Y. Mori, E. Ohmichi, S. Ikeda, S. NishiZaki, S. Nakatsuji, *Phys. Rev. Lett.* **1998**, *81*, 3765.
[125] P. Maksymovych, S. Jesse, P. Yu, R. Ramesh, A. P. Baddorf, S. V. Kalinin, *Science* **2009**, *324*, 1421.
[126] M. Lenzlinger, E. Snow, *J. Appl. Phys.* **1969**, *40*, 278.
[127] H. Kohlstedt, N. Pertsev, J. R. Contreras, R. Waser, *Phys. Rev. B* **2005**, *72*, 125341.
[128] S. W. Cheong, M. Mostovoy, *Nat. Mater.* **2007**, *6*, 13.
[129] N. A. Spaldin, S. W. Cheong, R. Ramesh, *Phys. Today* **2010**, *63*, 38.
[130] P. M. Chaikin, T. C. Lubensky, *Principles of Condensed Matter Physics*, Cambridge University Press, Cambridge, UK **2000**.
[131] A. A. Fraisse, C. Ringeval, D. N. Spergel, F. R. Bouchet, *Phys. Rev. D* **2008**, *78*, 043535.
[132] T. Choi, Y. Horibe, H. T. Yi, Y. J. Choi, W. Wu, S. W. Cheong, *Nat. Mater.* **2010**, *9*, 253.
[133] S. C. Chae, Y. Horibe, D. Y. Jeong, S. Rodan, N. Lee, S.-W. Cheong, *Proc. Natl. Acad. Sci. USA* **2010**, *107*, 21366.
[134] W. C. Koehler, H. L. Yakela, W. E. O. J. W. Cable, *Phys. Lett.* **1964**, *9*, 93.
[135] S. C. Abrahams, *Acta Crystallogr., B* **2001**, *57*, 485.
[136] B. B. van Aken, T. T. M. Palstra, A. Filippetti, N. A. Spaldin, *Nat. Mater.* **2004**, *3*, 164.
[137] C. J. Fennie, K. M. Rabe, *Phys. Rev. B* **2005**, *72*, 100103(R).
[138] M. Šafránková, J. Fousek, S. A. KiŽaev, *Czech. J. Phys.* **1967**, *17*, 559.
[139] W. S. Choi, S. J. Moon, S. Seok, A. Seo, D. Lee, J. H. Lee, P. Murugavel, T. W. Noh, Y. S. Lee, *Phys. Rev. B* **2008**, *78*, 054440.
[140] W. Wu, J. R. Guest, Y. Horibe, S. Park, T. Choi, S. W. Cheong, M. Bode, *Phys. Rev. Lett.* **2010**, *104*, 217601.
[141] M. Dawber, K. M. Rabe, J. F. Scott, *Rev. Mod. Phys.* **2005**, *77*, 1083.
[142] T. Jungk, Á. Hoffmann, M. Fiebig, E. Soergel, *Appl. Phys. Lett.* **2010**, *97*, 012904.
[143] E. B. Lochocki, S. Park, N. Lee, S.-W. Cheong, W. Wu, *Appl. Phys. Lett.* **2011**, *99*, 232901.
[144] W. Zhong, R. D. King-Smith, D. Vanderbilt, *Phys. Rev. Lett.* **1994**, *72*, 3618.
[145] M. E. Lines, A. M. Glass, *Principles and Applications of Ferroelectrics and Related Materials*, Oxford University Press, Oxford **1977**.
[146] A. Krishnan, M. M. J. Treacy, M. E. Bisher, P. Chandra, P. B. Littlewood, *AIP Conf. Proc.* **2000**, *535*, 191.
[147] V. Y. Shur, E. L. Rumyantsev, E. V. Nikolaeva, E. I. Shishkin, *Appl. Phys. Lett.* **2000**, *77*, 3636.
[148] C. L. Jia, S. B. Mi, K. Urban, I. Vrejoiu, M. Alexe, D. Hesse, *Nat. Mater.* **2008**, *7*, 57.
[149] X. Wu, D. Vanderbilt, *Phys. Rev. B* **2006**, *73*, 020103.
[150] P. De Wolf, J. Snauwaert, L. Hellemans, T. Clarysse, W. Vandervorst, M. D'Olieslaeger, D. Quaeyhaegens, *J. Vac. Sci. Technol. A* **1995**, *13*, 1699.
[151] T. Jungk, Á. Hoffmann, E. Soergel, *New J. Phys.* **2009**, *11*, 033029.
[152] G. V. S. Rao, B. M. Wanklyn, C. N. R. Rao, *J. Phys. Chem. Solids* **1971**, *32*, 345.
[153] M. Y. Gureev, A. K. Tagantsev, N. Setter, *Phys. Rev. B* **2011**, *83*, 184104.
[154] E. A. Eliseev, A. N. Morozovska, G. S. Svechnikov, V. Gopalan, V. Y. Shur, *Phys. Rev. B* **2011**, *83*, 235313.
[155] D. C. Tsui, H. L. Stormer, A. C. Gossard, *Phys. Rev. Lett.* **1982**, *48*, 1559.
[156] A. Ohtomo, H. Y. Hwang, *Nature* **2004**, *427*, 423.
[157] V. Garcia, M. Bibes, L. Bocher, S. Valencia, F. Kronast, A. Crassous, X. Moya, S. Enouz-Vedrenne, A. Gloter, D. Imhoff, C. Deranlot, N. D. Mathur, S. Fusil, K. Bouzehouane, A. Barthélémy, *Science* **2010**, *327*, 1106.
[158] A. Lubk, S. Gemming, N. A. Spaldin, *Phys. Rev. B* **2009**, *80*.
[159] G. I. G. I. I. Ivanchik, N. F. Kovtoniuk, *Sov. Phys. Solid State* **1969**, *11*, 1956.
[160] J. Hlinka, P. Márton, *Phys. Rev. B* **2006**, *74*, 104104.
[161] P. Marton, I. Rychetsky, J. Hlinka, *Phys. Rev. B* **2010**, *81*, 144125.
[162] V. Stepkova, P. Marton, J. Hlinka, *J. Phys. Cond. Matt.* **2012**, *24*, 212201.
[163] E. A. Eliseev, P. V. Yudin, S. V. Kalinin, N. Setter, A. K. Tagantsev, A. N. Morozovska, *Arxiv Condensed Matter Materials Science* **2012**.
[164] A. K. Tagantsev, *Phys. Rev. B* **1986**, *34*, 5883.
[165] V. S. Mashkevich, K. B. Tolpygo, *Zh. Eksp. Teor. Fiz.* **1957**, *31*, 520
[166] S. Kogan, *Sov. Phys. Solid State* **1964**, *5*, 2069.
[167] G. Catalan, L. J. Sinnamon, J. M. Gregg, *J. Phys. Cond. Matt.* **2004**, *16*, 2253.
[168] G. Catalan, B. Noheda, J. McAneney, L. J. Sinnamon, J. M. Gregg, *Phys. Rev. B* **2005**, *72*, 020102.
[169] R. Maranganti, N. D. Sharma, P. Sharma, *Phys. Rev. B* **2006**, *74*, 014110.
[170] M. S. Majdoub, T. Cagin, P. Sharma, *Phys. Rev. B* **2008**, *77*, 125424.
[171] M. S. Majdoub, R. Maranganti, P. Sharma, *Phys. Rev. B* **2009**, *79*, 115412.
[172] E. A. Eliseev, A. N. Morozovska, M. D. Glinchuk, R. Blinc, *Phys. Rev. B* **2009**, *79*, 165433.
[173] A. N. Morozovska, E. A. Eliseev, G. S. Svechnikov, S. V. Kalinin, *Phys. Rev. B* **2011**, *84*, 045402
[174] M. Gharbi, Z. Sun, P. Sharma, K. White, *Appl. Phys. Lett.* **2009**, *95*, 142901.
[175] A. K. Tagantsev, V. Meunier, P. Sharma, *MRS Bull.* **2009**, *34*, 643.
[176] P. V. Yudin, A. K. Tagantsev, E. A. Eliseev, A. N. Morozovska, N. Setter, *Phys. Rev. B* **2012**, *86*, 134102.
[177] A. K. Tagantsev, G. Gerra, *J. Appl. Phys.* **2006**, *100*, 051607.
[178] J. M. Ziman, *Principles of the Theory of Solids*, Cambridge University Press, Cambridge **1972**.
[179] G. L. Bir, G. E. Pikus, *Symmetry and Strain-Induced Effects in Semiconductors*, Wiley/Halsted Press, New York, **1974**, 484.
[180] G. A. Korn, T. M. Korn, *Mathematical Handbook for Scientists and Engineers*, McGraw-Hill, New York **1961**.
[181] J. Přívratská, V. Janovec, *Ferroelectrics* **1997**, *204*, 321.
[182] J. Přívratská, V. Janovec, *Ferroelectrics* **1999**, *222*, 23.
[183] J. Přívratská, B. Shaparenko, V. Janovec, D. Litvin, *Ferroelectrics* **2002**, *269*, 39.
[184] S. Artyukhin, K. T. Delaney, N. A. Spaldin, M. Mostovoy, *arXiv.org, e-Print Arch., Condens. Matter* **2012**, *arXiv:*1204.3785.
[185] A. Gruverman, D. Wu, H. J. Fan, I. Vrejoiu, M. Alexe, R. J. Harrison, J. F. Scott, *J. Phys.: Condens. Matter* **2008**, *20*, 342201.
[186] B. J. Rodriguez, X. S. Gao, L. F. Liu, W. Lee, I. I. Naumov, A. M. Bratkovsky, D. Hesse, M. Alexe, *Nano Lett.* **2009**, *9*, 1127.
[187] Y. Ivry, D. P. Chu, J. F. Scott, C. Durkan, *Phys. Rev. Lett.* **2010**, *104*, 207602.
[188] L. J. McGilly, A. Schilling, J. M. Gregg, *Nano Lett.* **2010**, *10*, 4200.
[189] I. Naumov, H. Fu, *Phys. Rev. Lett.* **2007**, *98*, 077603.
[190] Z. Wu, N. Huang, Z. Liu, J. Wu, W. Duan, B.-L. Gu, *J. Appl. Phys.* **2007**, *101*, 014112.
[191] J. Slutsker, A. Artemev, A. Roytburd, *Phys. Rev. Lett.* **2008**, *100*, 087602.
[192] S. Prosandeev, I. Ponomareva, I. Naumov, I. Kornev, L. Bellaiche, *J. Phys. Condens. Matter* **2008**, *20*, 193201.
[193] J. Wang, *Appl. Phys. Lett.* **2010**, *97*, 192901.
[194] C.-L. Jia, K. W. Urban, M. Alexe, D. Hesse, I. Vrejoiu, *Science* **2011**, *331*, 1420.

[195] C. T. Nelson, B. Winchester, Y. Zhang, S.-J. Kim, A. Melville, C. Adamo, C. M. Folkman, S.-H. Baek, C.-B. Eom, D. G. Schlom, L.-Q. Chen, X. Pan, *Nano Lett.* **2011**, *11*, 828.

[196] A. Schilling, D. Byrne, G. Catalan, K. G. Webber, Y. A. Geneko, G. S. Wu, J. F.Scott, J.M.Gregg, *Nano Lett.* **2009**, *9*, 3359.

[197] N. Balke, S. Choudhury, S. Jesse, M. Huijben, Y. H. Chu, A. P. Baddorf, L. Q. Chen, R. Ramesh, S. V. Kalinin, *Nat. Nanotechnol.* **2009**, *4*, 868.

[198] R. K. Vasudevan, Y.-C. Chen, H.-H. Tai, N. Balke, P. Wu, S. Bhattacharya, L. Q. Chen, Y.-H. Chu, I. N. Lin, S. V. Kalinin, V. Nagarajan, *ACS Nano* **2011**, *5*, 879.

[199] R. K. Vasudevan, Y. Liu, J. Li, W.-I. Liang, A. Kumar, S. Jesse, Y.-C. Chen, Y.-H. Chu, V. Nagarajan, S. V. Kalinin, *Nano Lett.* **2011**, *11*, 3346.

[200] A. Gruverman, D. Wu, H. J. Fan, I. Vrejoiu, M. Alexe, R. J. Harrison, J. F. Scott, *J. Phys. Condens. Matter* **2008**, *20*, 342201.

[201] S. Chae, Y. Horibe, D. Jeong, S. Rodan, N. Lee, S. W. Cheong, *Proc. Nat. Acad. Sci. USA* **2010**, *107*, 21366.

[202] K. Y. Guslienko, V. Novosad, Y. Otani, H. Shima, K. Fukamichi, *Appl. Phys. Lett.* **2001**, *78*, 3848.

[203] S. Prosandeev, L. Bellaiche, *Phys. Rev. B* **2007**, *75*, 094102.

[204] M. Schneider, H. Hoffmann, J. Zweck, *Appl. Phys. Lett.* **2001**, *79*, 3113.

[205] D. Sichuga, W. Ren, S. Prosandeev, L. Bellaiche, *Phys. Rev. Lett.* **2010**, *104*, 207603.

[206] J. B. Neaton, C. Ederer, U. V. Waghmare, N. A. Spaldin, K. M. Rabe, *Phys. Rev. B* **2005**, *71*, 014113.

[207] V. Anbusathaiah, D. Kan, F. C. Kartawidjaja, R. Mahjoub, M. A. Arredondo, S. Wicks, I. Takeuchi, J. Wang, V. Nagarajan, *Adv. Mater.* **2009**, *21*, 3497.

[208] A. Borisevich, O. S. Ovchinnikov, H. J. Chang, M. P. Oxley, P. Yu, J. Seidel, E. A. Eliseev, A. N. Morozovska, R. Ramesh, S. J. Pennycook, S. V. Kalinin, *ACS Nano* **2010**, *4*, 6071.

[209] S. Van Aert, S. Turner, R. Delville, D. Schryvers, G. Van Tendeloo, E. K. H. Salje, *Adv. Mater.* **2012**, *24*, 523.

[210] J. Kling, X. Tan, W. Jo, H. J. Kleebe, H. Fuess, J. Rödel, *J. Am. Ceram. Soc.* **2010**, *93*, 2452.

[211] X. Tan, Z. Xu, J. K. Shang, *Mater. Sci. Eng., A* **2001**, *314*, 157.

[212] C. T. Nelson, P. Gao, J. R. Jokisaari, C. Heikes, C. Adamo, A. Melville, S. H. Baek, C. M. Folkman, B. Winchester, Y. Gu, *Science* **2011**, *334*, 968.

[213] H.-J. Chang, S. V. Kalinin, S.-Y. Yang, P. Yu, S. Bhattacharya, P.-P. Wu, N. Balke, S. Jesse, L.-Q. Chen, R. Ramesh, S. J. Pennycook, A. Y. Borisevich, *J. Appl. Phys.* **2011**, *110*, 052014.